

# Finding graph isomorphisms in heated spaces in almost no time\*

Sara Najem

Department of Physics

Complexity and Network Science Cluster, CAMS

American University of Beirut, Lebanon

sn62@aub.edu.lb

Amer E. Mouawad

Department of Computer Science

Complexity and Network Science Cluster, CAMS

American University of Beirut, Lebanon

aa368@aub.edu.lb

## Abstract

Graph isomorphism, the problem of determining whether two graphs encode the same combinatorial structure, has long challenged attempts at a purely structural resolution. We introduce a deterministic framework that approaches isomorphism through multi-scale diffusion coupled to geometry, establishing a direct connection between discrete spectral geometry and algorithmic symmetry breaking. Each vertex is assigned a curvature-like signature derived from the short-time behavior of a (possibly fractional) graph Laplacian heat kernel, with dependence on spectral dimension. These signatures induce canonical vertex partitions that drive systematic symmetry reduction.

Refinement proceeds in two stages. First, curvature-based signatures are aggregated to form equivalence classes of the original vertices. If non-singleton classes remain, refinement is strengthened through structured probing: selected vertices are temporarily augmented with controlled gadgets, and the induced partitions are compared to produce refined probe profiles. If termination has not been reached after this refinement stage, only then, vertices are deterministically individualized through synchronized, permanent structural augmentation. These augmentations accumulate monotonically, yielding a geometry-guided individualization–refinement hierarchy. The latter leads to the elimination of symmetry through geometric amplification rather than combinatorial search.

Across extensive experiments, including random graphs, strongly regular graphs, and established benchmark graphs, the framework consistently resolves instances that challenge classical spectral and refinement-based techniques. Beyond isomorphism, the results position diffusion-based curvature as a fundamental structural descriptor of networks and introduce a new geometric paradigm for symmetry resolution in discrete systems.

**Keywords:** graph isomorphism; spectral geometry; Laplacian heat kernel; discrete curvature; symmetry breaking

---

\*Source code for our implementation available at <https://github.com/s-najem/Isomorphism-Graph-Curvature>.

# Contents

<b>1</b>	<b>Introduction</b>	<b>4</b>
<b>2</b>	<b>Background and related work</b>	<b>5</b>
2.1	Graph Laplacians, diffusion, and spectral geometry . . . . .	5
2.2	Spectral methods and graph isomorphism . . . . .	6
2.3	Combinatorial refinement and algorithmic complexity . . . . .	6
2.4	Diffusion geometry as a refinement engine . . . . .	6
<b>3</b>	<b>The base algorithm for computing curvatures</b>	<b>7</b>
3.1	Laplacian and heat kernel . . . . .	7
3.2	Spectral dimension and short-time regime . . . . .	7
3.3	Curvature extraction from short-time expansion . . . . .	8
3.4	Breaking symmetric configurations and fractional scaling . . . . .	8
3.5	Role of the base geometric pipeline . . . . .	9
<b>4</b>	<b>From local curvature to BFS-curvature signatures</b>	<b>9</b>
4.1	Definition of BFS-curvature signatures . . . . .	10
4.2	Multi-scale geometric interpretation . . . . .	10
4.3	Induced equivalence classes . . . . .	10
4.4	Increasing geometric resolution . . . . .	11
4.5	Role in the overall algorithm . . . . .	11
<b>5</b>	<b>Geometric normalization, refinement, and vertex individualization</b>	<b>11</b>
5.1	Geometric normalization via subdivision . . . . .	12
5.2	Structured probing as refinement . . . . .	12
5.3	Deterministic individualization . . . . .	12
5.4	Refinement strategy and termination . . . . .	13
5.5	Interpretation . . . . .	13
<b>6</b>	<b>The complete algorithm for graph isomorphism</b>	<b>13</b>
6.1	Algorithm overview . . . . .	13
6.2	Probe gadgets, probe outcomes, and probe profiles . . . . .	15
6.3	Deterministic individualization by permanent augmentation . . . . .	17
6.4	Termination and correctness . . . . .	17
<b>7</b>	<b>Time and space complexity</b>	<b>18</b>
7.1	Working-graph size under worst-case augmentation . . . . .	18
7.2	Cost of one spectral-geometric evaluation . . . . .	19
7.3	Cost of BFS-curvature signature construction . . . . .	19
7.4	Worst-case cost of structured probing (triplets) . . . . .	19
7.5	Worst-case number of rounds . . . . .	19
7.6	Total worst-case time bound . . . . .	19
7.7	Worst-case space bound . . . . .	20
7.8	Verification cost . . . . .	20
<b>8</b>	<b>Implementation details</b>	<b>20</b>

<b>9</b>	<b>Experimental results</b>	<b>23</b>
9.1	Randomly generated instances . . . . .	23
9.1.1	Random geometric graphs . . . . .	26
9.1.2	Power-law cluster graphs . . . . .	27
9.1.3	Stochastic block graphs . . . . .	28
9.1.4	Regular graphs . . . . .	29
9.1.5	Albert–Barabási graphs . . . . .	29
9.1.6	Watts–Strogatz graphs . . . . .	31
9.1.7	Erdős–Rényi graphs . . . . .	32
9.1.8	Tree graphs . . . . .	33
9.1.9	Paley graphs . . . . .	34
9.2	Known benchmark graphs . . . . .	36
9.2.1	Experimental protocol . . . . .	36
9.2.2	Affine geometry graphs . . . . .	36
9.2.3	Cai–Fürer–Immerman graphs . . . . .	37
9.2.4	Miyazaki graphs . . . . .	38
9.2.5	Grid graphs . . . . .	39
9.2.6	Hadamard matrix graphs . . . . .	40
9.2.7	Latin square graphs . . . . .	41
9.2.8	Lattice graphs . . . . .	41
9.2.9	Additional Paley graphs . . . . .	41
9.2.10	Desarguesian projective plane graphs . . . . .	42
9.2.11	Steiner triple system graphs . . . . .	43
9.2.12	Triangular graphs (triang) . . . . .	43
9.2.13	Dawar–Yeung graphs (sat_cfi) . . . . .	43
<b>10</b>	<b>Conclusion and future work</b>	<b>44</b>

# 1 Introduction

The graph isomorphism problem asks whether two finite graphs admit a bijection between their vertex sets that preserves adjacency. Despite decades of study, it occupies a singular position in complexity theory: it is neither known to admit a general polynomial-time algorithm nor believed to be NP-complete. Beyond its theoretical significance, graph isomorphism underlies applications ranging from chemical structure analysis to large-scale network comparison. The central challenge is symmetry resolution; distinguishing vertices in the presence of potentially large automorphism groups without resorting to exhaustive search.

Most practical algorithms address this challenge through progressive refinement. Vertices are grouped into equivalence classes using combinatorial invariants, and these classes are iteratively refined using increasingly detailed structural information. If refinement separates all vertices into singletons, a canonical bijection is obtained and verified directly. This paradigm underlies influential procedures such as Weisfeiler–Leman refinements and their extensions. However, purely combinatorial refinement can stabilize on highly symmetric graph families, leaving substantial ambiguity unresolved.

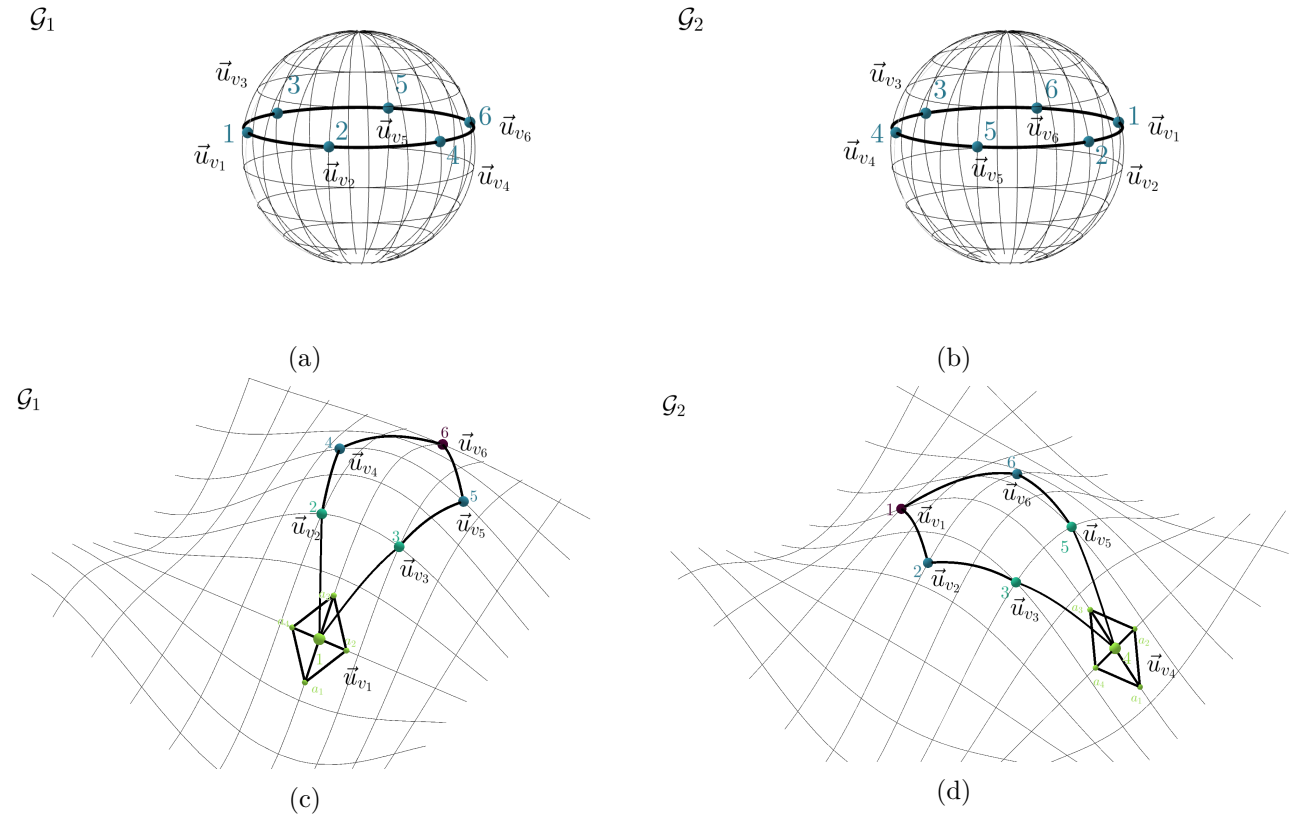


Figure 1: The geometric signatures of the vertices  $u_v$  of two cycles  $\mathcal{G}_1$  and  $\mathcal{G}_2$  are shown. The signatures are all equal making the nodes indistinguishable and part of one equivalence class. Symmetry is broken by attaching a clique to vertex 1 in  $\mathcal{G}_1$  and vertex 4 in  $\mathcal{G}_2$ , which allows their identification through their BFS-curvature signatures. The process is repeated iteratively on the remaining indistinguishable vertices.

Here we introduce a deterministic refinement framework driven by diffusion geometry. The short-time behavior of heat diffusion encodes multi-scale structural information that can systematically break symmetry. Each vertex is assigned a curvature-like signature derived from a (possibly fractional) graph Laplacian heat kernel, scaled by its spectral dimension. These signatures induce canonical equivalence classes of the original vertices and provide a geometric description of local structure that coherently propagates across the graph.

Refinement proceeds iteratively. First, diffusion-based signatures are aggregated over expanding neighborhoods to form vertex equivalence classes. If non-singleton classes remain, refinement is strengthened through structured probing: selected vertices from the smallest unresolved class are temporarily augmented with controlled gadgets, and the induced partitions of the probed graphs are compared. This probing phase refines the candidate class by grouping vertices according to their probe profiles, revealing asymmetries not detected by intrinsic diffusion alone.

Only after this refinement stage, if the partition still contains non-singleton classes that are not certified twin structures, does the algorithm perform deterministic individualization. Guided by the refined probe partition, matched vertices in the two graphs are permanently augmented in a synchronized and monotone manner. Diffusion-based refinement then resumes on the enriched graphs. The procedure terminates when every original class is either a singleton or a symmetric twin class. In both cases, a vertex bijection consistent with the induced partition is constructed and explicitly verified on the original input graphs, guaranteeing one-sided correctness (see Figure 1).

We evaluate the framework on diverse graph families, including random graphs, strongly regular graphs, and established benchmark instances. Across all tested cases, including highly symmetric constructions that challenge classical spectral and refinement-only methods, the procedure successfully resolves isomorphism.

More broadly, this work advances a geometric perspective on symmetry resolution. It demonstrates that multi-scale diffusion geometry can serve as a systematic engine for refinement, introducing a deterministic, geometry-guided alternative to purely combinatorial or search-based approaches to graph isomorphism and related symmetry-detection problems.

## 2 Background and related work

### 2.1 Graph Laplacians, diffusion, and spectral geometry

The graph Laplacian provides a fundamental analytic representation of a discrete structure. Given a simple undirected connected graph  $\mathcal{G} = (V, E)$  with adjacency matrix  $A$  and degree matrix  $D$ , the (combinatorial) Laplacian is defined as

$$L = D - A.$$

The matrix  $L$  is symmetric and positive semidefinite, with real, nonnegative eigenvalues. Its nullspace is spanned by indicator vectors of connected components, and the multiplicity of the zero eigenvalue equals the number of connected components [23, 9].

The spectrum of  $L$  encodes structural information at multiple scales. The second-smallest eigenvalue (algebraic connectivity) reflects global expansion properties [14, 3], while the full spectrum governs diffusion, random walks, and mixing processes [11, 25]. These connections justify interpreting  $L$  as a discrete analogue of the Laplace–Beltrami operator on a Riemannian manifold.

Diffusion on a graph is governed by the heat equation

$$\frac{\partial u}{\partial t} = -Lu,$$

whose solution is given by the heat kernel  $K(t) = e^{-tL}$ . The heat kernel interpolates between local and global structure: small values of  $t$  probe immediate neighborhoods, whereas larger values reflect long-range connectivity [22]. In continuous geometry, short-time heat asymptotics encode intrinsic quantities such as dimension and curvature [27]. This motivates extracting analogous geometric descriptors from discrete diffusion processes.

Fractional Laplacians extend this framework by spectrally scaling eigenvalues  $\lambda_i \mapsto \lambda_i^s$  for  $s > 0$ , to account for non-locality. Such scaling modifies diffusion rates across frequency bands and has been studied in anomalous transport, and complex networks [2, 8, 30]. Closely related is the notion of spectral dimension, which characterizes the asymptotic scaling of eigenvalue density near zero. In the present work the spectral dimension plays an important role in defining heat-kernel scaling across graph families.

## 2.2 Spectral methods and graph isomorphism

Because the Laplacian is invariant under vertex relabeling, spectral quantities are natural graph invariants. If two graphs are isomorphic, their Laplacians are related by conjugation with a permutation matrix and therefore share identical spectra [23]. Spectral mismatch thus certifies non-isomorphism.

However, spectral equality does not imply isomorphism. Infinite families of non-isomorphic cospectral graphs are known [23], demonstrating that eigenvalues alone are insufficient to capture full combinatorial structure. This limitation parallels classical questions in spectral geometry concerning the extent to which geometric structure is determined by eigenvalues.

Despite these limitations, spectral information is widely used in practical isomorphism testing. Eigenvectors provide geometric embeddings of vertices, and heat-kernel-based descriptors yield multi-scale vertex signatures [29, 32, 28]. More recent approaches aggregate spectral information across eigenmodes to increase discriminative power [12]. These developments indicate that while raw spectra are incomplete invariants, structured spectral descriptors can serve as powerful refinement tools.

## 2.3 Combinatorial refinement and algorithmic complexity

Combinatorial refinement is central to modern isomorphism solvers. The Weisfeiler–Leman (WL) hierarchy iteratively refines vertex colors based on neighborhood structure and is highly effective in practice [36]. Nevertheless, WL refinement can stabilize on highly symmetric graph families, including strongly regular graphs [4, 34], leaving substantial ambiguity unresolved.

From a complexity perspective, graph isomorphism is polynomial-time solvable for numerous restricted classes, including trees [1], bounded-degree graphs [19], planar graphs [17], and bounded treewidth graphs [16]. Babai’s quasipolynomial-time algorithm established a general upper bound of  $n^{O(\log^c n)}$  for all graphs [5]. However, the existence of a deterministic polynomial-time algorithm for general graph isomorphism remains an open question.

## 2.4 Diffusion geometry as a refinement engine

The preceding discussion highlights a recurring obstacle: persistent symmetry. Both combinatorial refinement and coarse spectral invariants may fail when local structure is highly regular. The difficulty lies not in graph size but in the inability of refinement mechanisms to propagate asymmetries.

This observation motivates integrating diffusion and geometry directly into the refinement process. Short-time heat diffusion encodes subtle structural distinctions that may be invisible to purely combinatorial statistics. By organizing diffusion-derived signatures into deterministic refinement steps, and strengthening refinement via controlled probing when necessary, one can attempt to transform geometric information into a systematic symmetry-breaking mechanism.

The present work develops this idea into a concrete algorithmic framework. Diffusion-based signatures define initial equivalence classes; structured probing refines unresolved classes; and deterministic (geometric) individualization applies synchronized augmentations when refinement alone is insufficient. In contrast to approaches that use spectral data only as auxiliary invariants, diffusion and geometry here serve as the primary driver of refinement.

### 3 The base algorithm for computing curvatures

We begin by describing the geometric core of our framework. At this stage, the algorithm operates purely at the level of local diffusion and its relation to geometry. It does not construct vertex correspondences or refine equivalence classes. Instead, it extracts canonical curvature-like descriptors from the graph Laplacian that serve as the foundational invariants for all subsequent refinement stages.

#### 3.1 Laplacian and heat kernel

Let  $\mathcal{G} = (V, E)$  be a simple, undirected, connected graph with  $|V| = n$ . Let  $A$  denote its adjacency matrix and  $D$  its degree matrix. The combinatorial Laplacian is defined by  $L = D - A$ . The matrix  $L$  is symmetric and positive semidefinite and admits an orthonormal eigenbasis [23, 25, 11]. Let  $L = V^\top \Lambda V$ , where  $\Lambda = \text{diag}(\lambda_1, \dots, \lambda_n)$  and  $V$  contains the corresponding eigenvectors.

Diffusion on the graph is governed by the heat equation

$$\frac{\partial u}{\partial t} = -Lu,$$

whose solution is given by the heat kernel  $K(t) = e^{-tL} = V^\top e^{-t\Lambda} V$ . The diagonal entries  $K(i, i, t)$  represent heat-return probabilities at vertex  $i$ . These quantities encode local diffusion behavior across scales and form the basis of our geometric descriptors. Diffusion processes on networks and their spectral interpretation are well studied in both graph theory and network science [11, 21, 22].

Because  $L$  is defined canonically from  $\mathcal{G}$ , the heat kernel is equivariant under vertex relabeling. Any vertex permutation conjugates  $L$  and therefore transforms  $K(t)$  accordingly, ensuring that all derived quantities are graph invariants.

#### 3.2 Spectral dimension and short-time regime

The short-time behavior of the heat kernel depends on how the Laplacian spectrum scales near zero. To differentiate diffusion across graph families, we estimate the spectral dimension  $d_s$ , defined via the asymptotic scaling of the cumulative eigenvalue density [33], or equivalently the counting function

$$\rho(\lambda' < \lambda) \sim \lambda^{d_s/2} \quad \text{as } \lambda \rightarrow 0.$$

This notion originated in the study of diffusion on fractals and disordered media [2, 8] and has been extended to hierarchical and complex networks [31, 30, 18, 7].

In practice,  $d_s$  is estimated by linear regression on logarithmically scaled portions of the spectrum. The estimate is not itself used as a vertex-level invariant. Rather, it determines an appropriate short-time window in which diffusion primarily reflects local geometry rather than global mixing.

Time samples are chosen logarithmically within this short-time regime. In order to identify this short time interval, the trace of the heat kernel, defined as  $\text{Tr}(K)$ , is evaluated on the interval  $[1/\lambda_{max}, 1/\lambda_{min}]$ . The upper limit of the short time interval  $t^+$  is defined such that it maximizes the adjusted  $-R^2$  of the fit of  $\log \text{Tr}(K)$  versus time, while its lower limit is given by  $1/\lambda_{max}$ . This ensures stable coverage of multiple local scales while avoiding numerical instability at extremely small  $t$  and domination by global diffusion at larger  $t$ .

### 3.3 Curvature extraction from short-time expansion

On a manifold, in continuous Riemannian geometry, and close to  $t^+ \rightarrow 0$ , the heat kernel expansion is given by:

$$K(x, y, t) \sim \frac{1}{(4\pi t)^{n/2}} \exp\left(-\frac{d(x, y)^2}{4t}\right) \sum_{k=1}^{\infty} u_k(x, y) t^k, \quad (1)$$

with  $n$  denoting the dimension of the manifold,  $d(x, y)$  being the distance between arbitrary points in space and  $t$  is time. The diagonal heat kernel admits a short-time asymptotic expansion

$$K(x, x, t) \sim \frac{1}{(4\pi t)^{n/2}} \sum_{k=0}^{\infty} u_k(x) t^k,$$

where the Minakshisundaram-Pleijel coefficients  $u_k(x)$  encode geometric information such as curvature [27, 24, 10, 26]. It is well established that scalar curvature  $R(x)$ , which is the curvature at a given point in space, is given as the second term in the expansion, i.e., the coefficient that corresponds to  $k = 1$ .

Motivated by this analogy and by diffusion-based signatures in geometry processing [32, 29, 28], and taking  $x \rightarrow i$ , where the indices  $i$  denote the vertices' identities, we model the short-time behavior of  $K(i, i, t)$  by fitting a truncated expansion

$$K(i, i, t) \approx t^{-d_s/2} \sum_{k=0}^N u_k(i) t^k$$

over the selected short-time interval.

The coefficients  $u_k(i)$  are obtained via least-squares regression and serve as curvature-like descriptors of vertex  $i$ . Lower-order terms capture coarse diffusion geometry, while higher-order coefficients encode increasingly fine structural detail. Because they are derived canonically from the Laplacian spectrum and eigenvectors, these descriptors are equivariant under vertex relabeling.

For algorithmic robustness, coefficients are discretized via fixed scaling and rounding, yielding deterministic signatures suitable for cross-graph comparison.

### 3.4 Breaking symmetric configurations and fractional scaling

Purely local combinatorial refinement can fail in highly symmetric configurations. A simple example is a long cycle ( $n \geq 200$ ) with a small clique, i.e. a triangle, attached on some arbitrary vertex. Along the cycle, all vertices share identical local neighborhood structure. Vertices far away from the clique may remain indistinguishable under low-order combinatorial statistics. Classical Laplacian eigenvalues as well as curvature values, while globally informative, may also fail to provide sufficient vertex-level separation in such settings [23, 28].

This illustrates a broader limitation: under classical diffusion  $e^{-tL}$ , contributions from different spectral scales are fixed. Low-frequency eigenmodes dominate long-time behavior, while high-frequency modes decay rapidly. In graphs with extended regular regions, this can produce diffusion profiles that remain too uniform to separate vertices early in refinement.

To address this limitation, we also consider a spectrally scaled diffusion operator corresponding to a fractional graph Laplacian. Fractional Laplacians have been studied both theoretically [38, 37] and in applications to nonlocal network dynamics and graph learning [6, 20, 35]. Given eigenvalues  $\{\lambda_i\}$ , we define modified eigenvalues  $\mu_i = \lambda_i^s$ , for an exponent  $s > 0$ , and define the scaled heat kernel

$$K_s(t) = V^\top e^{-t \operatorname{diag}(\mu_1, \dots, \mu_n)} V.$$

When  $s = 1$ , classical diffusion is recovered. For  $s \neq 1$ , spectral bands are reweighted. If  $s < 1$ , low-frequency modes are relatively amplified, enhancing long-range sensitivity. If  $s > 1$ , higher-frequency components are emphasized, increasing sensitivity to fine local irregularities.

The exponent  $s$  is chosen in relation to the estimated spectral dimension, normalizing diffusion behavior across graph families with different effective dimensionality. Importantly, fractional scaling remains canonical: it modifies spectral weighting but introduces no external labeling or asymmetry.

Returning to the cycle-with-clique example, fractional scaling alters heat-return behavior. Under suitable scaling, deviations become detectable at lower polynomial orders in the short-time expansion than in the classical case. Thus vertices that are initially indistinguishable can separate purely through diffusion geometry.

### 3.5 Role of the base geometric pipeline

The base pipeline associates to each vertex  $i$  a finite vector

$$\mathbf{u}(i) = (u_0(i), \dots, u_K(i))$$

derived from short-time diffusion under (possibly fractional) spectral scaling.

These vectors provide canonical, multi-scale geometric fingerprints of vertices. While insufficient by themselves to resolve graph isomorphism in highly symmetric graphs, they establish the geometric quantities that drive all subsequent refinement, probing, and individualization stages. In the next sections, we show how these descriptors are aggregated and systematically amplified to form a deterministic refinement hierarchy.

## 4 From local curvature to BFS-curvature signatures

The curvature coefficients extracted by the base algorithm provide local geometric descriptors for individual vertices. However, local diffusion geometry alone is often insufficient to distinguish vertices in graphs with repetitive or highly regular structure. To propagate local information into a structured neighborhood context, we aggregate curvature data across graph neighborhoods using a breadth-first search (BFS) hierarchy.

This aggregation produces BFS-curvature signatures, which encode multi-scale diffusion geometry around each vertex in a canonical, distance-stratified manner. These signatures constitute the first refinement mechanism of the algorithm, transforming purely local descriptors into structured neighborhood-level invariants.

## 4.1 Definition of BFS-curvature signatures

Let  $\mathcal{G} = (V, E)$  denote the current working graph. The working graph may contain auxiliary vertices introduced during preprocessing or controlled perturbations. However, signatures are computed and compared only for the original vertices of the input graph.

Let  $u_k(i)$  denote the  $k$ -th heat-kernel coefficient at vertex  $i$ , and let

$$\mathbf{u}_K(i) = (u_0(i), u_1(i), \dots, u_K(i))$$

be the truncated curvature vector at order  $K$ . For deterministic comparison, each coefficient vector is discretized using a fixed scaling and rounding scheme.

For a vertex  $v$ , perform a BFS rooted at  $v$  in the working graph. This partitions vertices into layers

$$\mathcal{L}_0(v) = \{v\}, \quad \mathcal{L}_1(v), \quad \mathcal{L}_2(v), \quad \dots,$$

where  $\mathcal{L}_r(v)$  consists of vertices at graph distance  $r$  from  $v$ .

The BFS-curvature signature of  $v$  at truncation order  $K$  is defined as

$$\text{BCS}_K(v) = \left( \mathbf{u}_K(v), \text{sort}\{\mathbf{u}_K(w) : w \in \mathcal{L}_1(v)\}, \text{sort}\{\mathbf{u}_K(w) : w \in \mathcal{L}_2(v)\}, \dots \right),$$

where sorting within each layer is performed lexicographically.

The layer index encodes discrete distance from the root, while lexicographic sorting removes dependence on vertex labeling within each layer. Consequently,  $\text{BCS}_K(v)$  is canonically defined from graph structure and diffusion data and is equivariant under vertex relabeling.

## 4.2 Multi-scale geometric interpretation

The BFS-curvature signature can be interpreted as a discrete multi-scale geometric profile. The root contributes its intrinsic diffusion geometry, and successive BFS layers describe how this geometry interacts with increasingly distant neighborhoods.

Two vertices may share identical leading-order curvature coefficients yet differ in the organization of their surrounding diffusion profiles. By stratifying curvature data according to graph distance, BFS-curvature signatures capture both coefficient depth and spatial arrangement. As the truncation order  $K$  increases, the signatures incorporate increasingly fine local diffusion information. As BFS depth increases, the spatial extent of aggregation grows outward from the root. Together, these parameters provide two independent axes of geometric resolution.

The BFS-curvature signature is thus viewed as a discrete analogue of the local curvature profile of a point on a Riemannian manifold. In differential geometry, the full collection of curvature invariants (and their derivatives) at a point determines the local metric up to isometry (Cartan–Ambrose–Hicks theorem). Similarly,  $\text{BCS}(v)$  encodes the geometry of the metric-ball around  $v$  in the graph. Matching BFS-curvature signatures across two graphs is therefore analogous to constructing a global isometry: if every vertex in  $\mathcal{G}_1$  has an identical signature to some vertex in  $\mathcal{G}_2$ , then the two graphs share the same discrete metric structure. In effect, sorting and aligning the signatures from  $\mathcal{G}_1$  and  $\mathcal{G}_2$  “enforces” a discrete global isometry between the graphs.

## 4.3 Induced equivalence classes

For a fixed truncation order  $K$ , BFS-curvature signatures induce an equivalence relation on the original vertex set:

$$v \sim_K w \quad \text{if and only if} \quad \text{BCS}_K(v) = \text{BCS}_K(w).$$

This defines a partition of the original vertices into signature classes.

Given two graphs  $\mathcal{G}_1$  and  $\mathcal{G}_2$ , the multisets of signatures at order  $K$  are compared. If a signature appears with different multiplicities in the two graphs, they are deemed not isomorphic. If the induced partitions contain only singleton classes, a canonical bijection between vertices is determined by matching identical signatures.

If non-singleton classes persist and do not correspond to certified twin structures, the available geometric resolution is insufficient to fully distinguish vertices. In that case, refinement must continue.

#### 4.4 Increasing geometric resolution

Geometric resolution is increased deterministically by enlarging one or both of the following parameters:

- the truncation order  $K$  of the short-time expansion, and
- the BFS depth used in constructing the signature.

Both parameters are increased in a controlled, bounded manner. At each stage, the induced partition is recomputed and compared across graphs. Only when geometric refinement stabilizes without achieving termination does the algorithm proceed to structured probing. In our implementation, we let  $K$  and BFS depth be parameters, where  $K$  is set to 6 by default and BFS depth is set to infinity, i.e., BFS includes all vertices of the graph (since we assume connected graphs). We note here that disconnected graphs can easily be handled by adding a universal vertex, i.e., a vertex connected to all vertices of the input graphs.

#### 4.5 Role in the overall algorithm

BFS-curvature signatures form the primary intrinsic refinement mechanism of the algorithm. They propagate local diffusion geometry into structured, multi-scale invariants that refine vertex equivalence classes without modifying the graph.

Temporary probing, described in the next section, strengthens this refinement when intrinsic diffusion geometry alone is insufficient. Permanent individualization is invoked only after refinement, including probing, fails to achieve termination. This separation ensures that geometric information is fully exploited before structural augmentation is introduced.

## 5 Geometric normalization, refinement, and vertex individualization

BFS-curvature signatures provide a structured, multi-scale description of diffusion geometry around each vertex. In many graphs, these signatures refine all equivalence classes to singletons. However, at any fixed geometric resolution, multiple vertices may remain indistinguishable. Such degeneracies do not necessarily indicate the presence of automorphisms, nor do they imply failure of the method. They indicate only that the currently available geometric information is insufficient to separate certain vertices.

To address this, the algorithm applies a deterministic refinement hierarchy. Refinement is performed symmetrically on both input graphs and is interpreted exclusively through induced equivalence classes on the original vertex sets.

## 5.1 Geometric normalization via subdivision

Stable extraction of short-time diffusion coefficients requires an appropriate geometric scale. In certain graph families, particularly those with small diameter or strong regularity, diffusion may mix too rapidly to admit stable regression of curvature coefficients.

To regulate this behavior, the algorithm may apply bounded edge subdivision as a geometric normalization step. Each edge is replaced by a short path of fixed length, producing a subdivided graph. Subdivision is applied symmetrically to both input graphs and preserves isomorphism.

Subdivision vertices participate in diffusion and BFS-signature computations but are treated as auxiliary. They are excluded from equivalence-class comparison and from the final vertex correspondence. The subdivision depth is deterministically bounded by a polynomial in  $n$ .

## 5.2 Structured probing as refinement

If increasing coefficient depth and BFS aggregation fail to separate a non-singleton equivalence class  $\mathcal{C}$  of original vertices, refinement is strengthened through structured probing.

Probing is temporary and diagnostic. For a selected vertex  $u \in \mathcal{C}$ , augmented graphs are constructed in which carefully designed gadgets are attached to  $u$  together with other vertices in  $\mathcal{G}$ . The augmented graphs are processed through the same curvature and BFS-signature pipeline, and only the induced partitions on original vertices are retained. Auxiliary gadget vertices are discarded after each probe.

The primary probing mechanism operates on ordered vertex pairs. For each pair  $(u, v)$  with  $u \in \mathcal{C}$ ,  $v \in \mathcal{G}$ , and  $u \neq v$ , symmetric attachments are introduced in both graphs. These attachments combine a shared clique structure with private distinguishing components whose parameters are varied deterministically. Both orientations are evaluated to preserve symmetry under labeling.

For a fixed  $u$ , the multiset of induced refinement outcomes against all  $v \neq u$  defines a probe profile. Vertices in  $\mathcal{C}$  are partitioned according to equality of probe profiles. If this partition strictly refines  $\mathcal{C}$  while remaining consistent across the two graphs, the refinement is accepted.

If pair probing does not refine the class, the algorithm escalates to triplet probing. Triples  $(u, v, w)$  are augmented using three distinct private attachments, again evaluated under symmetric orientations. Triplet probing incorporates ternary structural relationships and increases discriminative power.

Probing refines equivalence classes but does not permanently modify the graphs. Permanent augmentation occurs only after refinement has produced a consistent partition that does not yet satisfy termination conditions.

## 5.3 Deterministic individualization

After refinement (including probing) is applied, the induced partition on original vertices is evaluated. If all classes are singletons or correspond to certified twin structures, the algorithm terminates. Otherwise, the algorithm performs deterministic vertex individualization.

Individualization consists of synchronized, permanent structural augmentation of matched vertices in the two graphs. Selected vertices, guided by the refined partition, are augmented with clique attachments or related structures. These augmentations accumulate monotonically across rounds and alter the working graphs for subsequent refinement.

Following individualization, geometric refinement (coefficient depth, BFS signatures, and probing) resumes on the enriched graphs.

## 5.4 Refinement strategy and termination

Refinement proceeds along three deterministically bounded axes:

1. heat-kernel coefficient depth,
2. BFS aggregation radius,
3. probing complexity (pair followed by triplet probing).

At each stage, equivalence classes on original vertices are recomputed and compared across the two graphs. Refinement is accepted only if induced partitions remain consistent. The algorithm terminates when:

- all original equivalence classes are singletons, or
- the remaining non-singleton classes correspond to provably symmetric twin vertices (true or false twins).

In either case, a vertex bijection consistent with the induced partition is constructed and explicitly verified on the original, unmodified graphs.

## 5.5 Interpretation

Refinement and probing are used solely to extract distinguishing information. Any candidate bijection induced by singleton or twin classes is explicitly verified on the original graphs by checking adjacency preservation. Consequently, the procedure is one-sidedly correct: it never declares two non-isomorphic graphs to be isomorphic. Failure to produce a verified bijection indicates only that the instance could not be resolved within the prescribed refinement bounds.

The refinement hierarchy can be viewed as progressively sharpening geometric resolution. At low resolution, diffusion may render distinct vertices indistinguishable. By increasing spectral depth, expanding spatial aggregation, and incorporating higher-order probing when necessary, the algorithm systematically amplifies latent asymmetries while maintaining determinism, symmetry, and polynomial bounds.

# 6 The complete algorithm for graph isomorphism

We now describe the complete deterministic procedure for graph isomorphism. The algorithm integrates diffusion-based curvature extraction, BFS-curvature aggregation, structured probing, and deterministic vertex individualization into a single refinement hierarchy. At every stage, both input graphs are processed symmetrically. All decisions are based solely on equivalence-class comparisons, and any candidate correspondence is accepted only after explicit verification on the original graphs.

## 6.1 Algorithm overview

Let  $\mathcal{G}_1 = (V_1, E_1)$  and  $\mathcal{G}_2 = (V_2, E_2)$  be connected graphs with  $|V_1| = |V_2| = n$ . We identify the original vertices with  $\{0, 1, \dots, n - 1\}$ . The algorithm maintains working graphs  $\tilde{\mathcal{G}}_1$  and  $\tilde{\mathcal{G}}_2$ , which may contain auxiliary vertices introduced by a one-time symmetric normalization step and by permanent individualization gadgets. Structured probing is performed on temporary copies and does not permanently modify  $\tilde{\mathcal{G}}_1, \tilde{\mathcal{G}}_2$ .

The procedure consists of a deterministic refinement loop. Algorithm 1 gives the high-level pseudocode; in what follows we define each component precisely.

---

**Algorithm 1** Proposed algorithm for graph isomorphism

---

**Require:** Connected graphs  $\mathcal{G}_1, \mathcal{G}_2$  on  $n$  vertices

**Ensure:** **isomorphic** with verified bijection, or **fail**

```
1: Determine minimal subdivision level  $s$  satisfying bounds and non-degenerate spectral dimension
2:  $\tilde{\mathcal{G}}_1 \leftarrow \text{SubdivideEveryEdge}(\mathcal{G}_1, s)$ 
3:  $\tilde{\mathcal{G}}_2 \leftarrow \text{SubdivideEveryEdge}(\mathcal{G}_2, s)$ 
4:  $q \leftarrow q_0$  ▷ initial gadget size
5: while true do
6:    $\Pi_1 \leftarrow \text{SignaturePartition}(\tilde{\mathcal{G}}_1)$  ▷ original-only signatures
7:    $\Pi_2 \leftarrow \text{SignaturePartition}(\tilde{\mathcal{G}}_2)$ 
8:   if  $\Pi_1, \Pi_2$  disagree in signature multiplicities then
9:     return fail
10:  if  $\Pi_1, \Pi_2$  are all singletons, or all non-singletons are matched twin classes then
11:     $f \leftarrow \text{CanonicalBijectionFromClasses}(\Pi_1, \Pi_2)$ 
12:    if  $\text{VerifyAdjacency}(\mathcal{G}_1, \mathcal{G}_2, f)$  then
13:      return isomorphic
14:    else
15:      return fail
16:     $(\mathcal{C}_1, \mathcal{C}_2) \leftarrow \text{SmallestMatchedNonSingletonClass}(\Pi_1, \Pi_2)$ 
17:     $R_1 \leftarrow \text{ProbeRefine}(\tilde{\mathcal{G}}_1, \mathcal{C}_1, q)$  ▷ pair then triplet
18:     $R_2 \leftarrow \text{ProbeRefine}(\tilde{\mathcal{G}}_2, \mathcal{C}_2, q)$ 
19:     $M \leftarrow \text{MatchRefinedGroupsByProfiles}(R_1, R_2)$ 
20:    if no singleton groups in both  $R_1$  and  $R_2$  then
21:       $(A, B) \leftarrow \text{SmallestMatchedGroupPair}(M)$ 
22:       $(u, v) \leftarrow \text{ChooseRepresentatives}(A, B)$ 
23:       $\tilde{\mathcal{G}}_1 \leftarrow \text{AttachClique}(\tilde{\mathcal{G}}_1, u, q)$ 
24:       $\tilde{\mathcal{G}}_2 \leftarrow \text{AttachClique}(\tilde{\mathcal{G}}_2, v, q)$ 
25:       $q \leftarrow q + 1$ 
26:    else
27:      for each matched singleton pair  $(u, v)$  in deterministic order do
28:         $\tilde{\mathcal{G}}_1 \leftarrow \text{AttachClique}(\tilde{\mathcal{G}}_1, u, q)$ 
29:         $\tilde{\mathcal{G}}_2 \leftarrow \text{AttachClique}(\tilde{\mathcal{G}}_2, v, q)$ 
30:         $q \leftarrow q + 1$ 
```

---

**Step 1: Initialization and symmetric normalization.** The algorithm first checks connectivity and fixed input bounds. If required, it applies a bounded symmetric normalization by subdividing every edge a common number of times  $s \geq 0$ . Starting from a prescribed  $s_0$ , it increases  $s$  until both subdivided graphs (i) lie within an allowed vertex-count window and (ii) yield a non-degenerate spectral-dimension estimate. This subdivision level is fixed and the resulting graphs become the initial working graphs  $\tilde{\mathcal{G}}_1, \tilde{\mathcal{G}}_2$ .

**Step 2: Curvature computation and signature partitioning.** On each refinement round and for each  $i \in \{1, 2\}$ :

- compute the Laplacian spectrum of  $\tilde{\mathcal{G}}_i$ ;
- estimate the spectral dimension;

- compute a fixed number of short-time curvature coefficients per vertex;
- construct BFS-curvature signatures for original vertices only (as defined previously).

This induces a partition  $\Pi_i$  of  $\{0, \dots, n-1\}$  into signature classes.

The partitions are compared across graphs by signature type and multiplicity. If some signature occurs with different multiplicity in  $\Pi_1$  and  $\Pi_2$ , the procedure terminates without success. Otherwise, refinement continues.

**Step 3: Termination conditions.** If every class in  $\Pi_1$  and  $\Pi_2$  is a singleton, the induced bijection is formed and verified explicitly on the original graphs  $\mathcal{G}_1, \mathcal{G}_2$  by adjacency preservation.

If non-singleton classes remain, the algorithm checks whether each such class is a twin class in the corresponding original graph: a non-singleton class  $\mathcal{C}$  is accepted as a true-twin class if all distinct  $u, v \in \mathcal{C}$  are adjacent and satisfy  $N(u) \setminus \mathcal{C} = N(v) \setminus \mathcal{C}$ , and as a false-twin class if all distinct  $u, v \in \mathcal{C}$  are non-adjacent and satisfy  $N(u) \setminus \mathcal{C} = N(v) \setminus \mathcal{C}$ . If, for every signature class, the twin-kind matches across  $\mathcal{G}_1$  and  $\mathcal{G}_2$ , a canonical bijection is constructed within each class (by deterministic ordering) and verified explicitly on  $\mathcal{G}_1, \mathcal{G}_2$ . If verification succeeds, the graphs are declared isomorphic; otherwise the algorithm fails.

**Step 4: Select a smallest unresolved matched class.** If termination is not reached, choose a smallest signature class  $\mathcal{C}_1$  in  $\Pi_1$  with  $|\mathcal{C}_1| \geq 2$  whose signature type appears in  $\Pi_2$  with the same size. Let  $\mathcal{C}_2$  denote the corresponding class in  $\Pi_2$ . Ties are broken deterministically (e.g., lexicographically by signature). The next refinement is focused on  $\mathcal{C}_1, \mathcal{C}_2$ .

**Step 5: Structured probing (temporary refinement).** Structured probing refines  $\mathcal{C}_1$  and  $\mathcal{C}_2$  by computing a probe profile for each candidate vertex. All probing is performed on temporary copies and discarded afterwards.

## 6.2 Probe gadgets, probe outcomes, and probe profiles

Fix an integer  $q \geq 1$  (the current gadget size parameter), and fix two distinct nonnegative path lengths  $\ell_u \neq \ell_v$ . A shared clique gadget attaches a fresh  $q$ -clique and connects every vertex in it to each endpoint in a given endpoint set. A private clique gadget of size  $t$  attached to  $x$  adds a fresh clique of size  $t$  and connects  $x$  to every vertex in that clique. A path gadget of length  $\ell$  attached to  $x$  adds a fresh simple path of  $\ell$  new vertices with one endpoint adjacent to  $x$  (and no other new edges).

**Pair probe construction.** Given a base graph  $\tilde{\mathcal{G}}$ , distinct original vertices  $u \neq v$ , parameters  $q$ , private clique sizes  $a \neq b$ , and path lengths  $\ell_u \neq \ell_v$ , define the temporary probed graph

$$H^{(2)}(\tilde{\mathcal{G}}; u, v; q, a, b, \ell_u, \ell_v)$$

as  $\tilde{\mathcal{G}}$  augmented by: (i) a shared  $q$ -clique connected to  $\{u, v\}$ , (ii) a private clique of size  $a$  attached to  $u$ , (iii) a private clique of size  $b$  attached to  $v$ , (iv) a path of length  $\ell_u$  attached to  $u$  and a path of length  $\ell_v$  attached to  $v$  (if the length is 0, no path is added).

Let  $\Pi(H^{(2)})$  be the induced original-only signature partition and let

$$\text{End}(H^{(2)}, x) := (\tau_x, s_x)$$

where  $\tau_x$  is the signature type of  $x$  in  $\Pi(H^{(2)})$  and  $s_x$  is the size of its signature class. Let

$$\text{TypeMultiset}(H^{(2)}) \quad \text{and} \quad \text{SizeMultiset}(H^{(2)})$$

denote respectively the sorted multiset of signature types of all original vertices and the sorted multiset of class sizes in  $\Pi(H^{(2)})$ .

The pair outcome key is then

$$\text{OK}^{(2)}(H^{(2)}; u, v) = \left( \text{canon}\{\text{End}(H^{(2)}, u), \text{End}(H^{(2)}, v)\}, \text{TypeMultiset}(H^{(2)}), \text{SizeMultiset}(H^{(2)}) \right),$$

where  $\text{canon}\{\cdot, \cdot\}$  denotes canonical ordering of the two endpoints (so that swapping  $u$  and  $v$  yields the same key). All outcome keys are computed from an original-only signature partition of the temporary probed graph.

**Triplet probe construction.** Given  $\tilde{\mathcal{G}}$  and distinct original vertices  $u, v, w$ , define the temporary probed graph

$$H^{(3)}(\tilde{\mathcal{G}}; u, v, w; q, a, b, c, \ell_u, \ell_v, \ell_w)$$

by attaching a shared  $q$ -clique to  $\{u, v, w\}$ , three distinct private cliques of sizes  $a, b, c$  at  $u, v, w$ , and three paths of pairwise distinct lengths  $\ell_u, \ell_v, \ell_w$  at  $u, v, w$ . Let  $\Pi(H^{(3)})$  be the induced original-only signature partition. The triplet outcome key is defined by

$$\text{OK}^{(3)}(H^{(3)}; u, v, w) = \left( \text{canon}\{\text{End}(H^{(3)}, u), \text{End}(H^{(3)}, v), \text{End}(H^{(3)}, w)\}, \right. \\ \left. \text{TypeMultiset}(H^{(3)}), \text{SizeMultiset}(H^{(3)}) \right).$$

where  $\text{canon}\{\cdot, \cdot, \cdot\}$  denotes canonical ordering of the three endpoints.

**Two-orientation symmetrization.** To make probing invariant to endpoint orientation, each probe uses two gadget assignments and records the unordered pair of resulting outcome keys.

- **Pairs.** Fix distinct private clique sizes  $(q+1, q+2)$  and distinct path lengths  $(\ell_u, \ell_v)$ . For each ordered pair  $(u, v)$ , compute

$$A = \text{OK}^{(2)}\left(H^{(2)}(\tilde{\mathcal{G}}; u, v; q, q+1, q+2, \ell_U, \ell_V); u, v\right),$$

$$B = \text{OK}^{(2)}\left(H^{(2)}(\tilde{\mathcal{G}}; u, v; q, q+2, q+1, \ell_V, \ell_U); u, v\right),$$

and let  $\text{POK}^{(2)}(u, v) := \text{canon}\{A, B\}$  be the unordered (canonicalized) pair of keys.

- **Triplets.** Fix private clique sizes  $(q+1, q+2, q+3)$ . Choose a third path length  $\ell_W \geq 0$  deterministically as the smallest nonnegative integer distinct from  $\ell_U$  and  $\ell_V$ . For each unordered  $\{v, w\}$  with  $v < w$  and  $v, w \neq u$ , compute two orientations obtained by swapping the private gadgets and path lengths assigned to  $v$  and  $w$ , producing keys  $A, B$ , and define  $\text{POK}^{(3)}(u, v, w) := \text{canon}\{A, B\}$ .

**Pair probe profile.** For a fixed candidate vertex  $u$ , its pair probe profile is the multiset of symmetrized pair outcomes over all  $v \neq u$ :

$$\text{PP}_{\tilde{\mathcal{G}}}^{(2)}(u; q, \ell_U, \ell_V) := \left\{ \left\{ \text{POK}^{(2)}(u, v) : v \in \{0, \dots, n-1\} \setminus \{u\} \right\} \right\},$$

where  $\{\{\cdot\}\}$  denotes a multiset. Equivalently, we represent the profile as a frequency map

$$\text{PP}_{\tilde{\mathcal{G}}}^{(2)}(u) : \text{POK}^{(2)} \mapsto \#\{v \neq u : \text{POK}^{(2)}(u, v) = \text{POK}^{(2)}\}.$$

**Triplet probe profile.** Analogously, the triplet probe profile is the multiset of symmetrized triplet outcomes over all unordered pairs  $\{v, w\}$  with  $v < w$  and  $v, w \neq u$ :

$$\text{PP}_{\tilde{\mathcal{G}}}^{(3)}(u; q, \ell_U, \ell_V) := \left\{ \left\{ \text{POK}^{(3)}(u, v, w) : v, w \in \{0, \dots, n-1\} \setminus \{u\}, v < w \right\} \right\},$$

or equivalently as its frequency map over distinct  $\text{POK}^{(3)}$  values.

**Probe-induced refinement of a class.** Given  $\mathcal{C} \subseteq \{0, \dots, n-1\}$ , probing partitions  $\mathcal{C}$  into subclasses by equality of probe profiles:

$$u \equiv v \iff \text{PP}_{\tilde{\mathcal{G}}}^{(\cdot)}(u) = \text{PP}_{\tilde{\mathcal{G}}}^{(\cdot)}(v).$$

Pair probing is attempted first; triplet probing is used only if pair probing yields a single group.

### 6.3 Deterministic individualization by permanent augmentation

After probing is performed on  $\mathcal{C}_1$  and  $\mathcal{C}_2$ , refined groups are matched across graphs by exact equality of probe profiles.

Permanent augmentation then proceeds deterministically:

- If probing yields no singleton refined groups in either graph, choose the smallest matched refined group pair and attach a permanent clique of size  $q$  to a fixed representative vertex in each graph.
- If probing yields singleton refined groups, attach permanent cliques of size  $q$  to *all* matched singleton pairs (in deterministic order).

The size parameter  $q$  is increased by 1 after each matched attachment, ensuring distinctiveness of successive augmentations. The working graphs  $\tilde{\mathcal{G}}_1, \tilde{\mathcal{G}}_2$  are updated permanently, and the procedure proceeds to the next iteration.

### 6.4 Termination and correctness

The algorithm declares isomorphism only after constructing a bijection  $f$  on original vertices and verifying adjacency preservation on the unmodified inputs  $\mathcal{G}_1$  and  $\mathcal{G}_2$ :

$$\forall 0 \leq u < v < n : \{u, v\} \in E_1 \iff \{f(u), f(v)\} \in E_2.$$

Hence it never declares two non-isomorphic graphs to be isomorphic. If it terminates without a verified bijection, it reports failure to resolve isomorphism under the enforced bounds and refinement regime.

## 7 Time and space complexity

We analyze the worst-case running time and memory usage of the algorithm by decomposing it into its principal components: (i) spectral–geometric computation, (ii) BFS-curvature signature construction and comparison, (iii) structured probing (triplets in the worst case), (iv) permanent individualization.

Let  $n = |V|$  and  $m = |E|$  denote the number of vertices and edges of the original input graphs. All bounds are worst-case under the standard RAM model with arithmetic on  $O(\log n)$ -bit integers.

**Worst-case assumptions used in this section.** We assume:

1. The number of subdivision rounds is a fixed constant, hence the working graph size after subdivision remains  $N = \Theta(n + m)$  up to constant factors. In particular, when  $m = \Theta(n^2)$  (dense graphs),  $N = \Theta(n^2)$ .
2. The algorithm performs at most  $n$  permanent individualization steps (clique attachments).
3. In every refinement round, pair probing fails and triplet probing is invoked.
4. Clique sizes and path lengths are initialized as constants but may increase as a function of  $n$  due to repeated individualizations; we therefore track their contribution to the working graph size explicitly.

### 7.1 Working-graph size under worst-case augmentation

Let  $\tilde{G}$  denote a working graph at some round. Let  $p$  be the number of permanent clique attachments performed so far, with  $p \leq n$  in the worst case. Let  $q_j$  be the clique size used in the  $j$ -th permanent attachment. Since  $q_j$  increases by 1 after each attachment and begins at a constant,

$$q_j = \Theta(j).$$

Each attachment adds  $\Theta(q_j)$  new vertices and  $\Theta(q_j^2)$  new edges (the clique itself), plus  $\Theta(q_j)$  incident edges to the attachment vertex. Therefore, after  $p$  attachments,

$$N(p) = n + O(m) + \sum_{j=1}^p \Theta(q_j) = n + O(m) + \Theta\left(\sum_{j=1}^p j\right) = n + O(m) + \Theta(p^2),$$

and

$$M(p) = m + \sum_{j=1}^p \Theta(q_j^2) = m + \Theta\left(\sum_{j=1}^p j^2\right) = m + \Theta(p^3).$$

In the worst case  $p = \Theta(n)$ , hence

$$N(p) = \Theta(n + m + n^2) = \Theta(m + n^2), \quad M(p) = \Theta(m + n^3).$$

For dense graphs ( $m = \Theta(n^2)$ ) this yields  $N = \Theta(n^2)$  and  $M = \Theta(n^3)$ . For sparse graphs ( $m = \Theta(n)$ ), this yields  $N = \Theta(n^2)$  and  $M = \Theta(n^3)$  as well; the permanent cliques dominate.

Finally, note that path gadgets added during probing are temporary and contribute only  $O(q_j)$  vertices/edges per probe instance; this does not change asymptotic bounds because the dominant term arises from the permanent clique growth captured above.

## 7.2 Cost of one spectral-geometric evaluation

In each refinement round, the algorithm performs a full Laplacian eigendecomposition on the current working graph (for each of the two graphs). Using dense linear algebra, for a graph with  $N$  vertices this costs

$$O(N^3) \text{ time and } O(N^2) \text{ space.}$$

All additional spectral-dimension estimation and coefficient extraction steps are lower order in  $N$  compared to  $O(N^3)$ .

Thus, a single spectral-geometric evaluation stage costs  $O(N^3)$  time and  $O(N^2)$  space per graph, and the same asymptotic bounds apply to the two-graph execution up to a constant factor.

## 7.3 Cost of BFS-curvature signature construction

Constructing signatures for all original vertices requires performing BFS explorations on the working graph. A BFS costs  $O(N + M)$ , hence performing BFS from all  $n$  original vertices costs

$$O(n(N + M)).$$

In the worst case, this is dominated by the spectral cost  $O(N^3)$  once  $N = \Omega(n^2)$ , which holds under the permanent clique growth.

## 7.4 Worst-case cost of structured probing (triplets)

Let  $\mathcal{C}$  be the selected unresolved class with  $|\mathcal{C}| = k$ . In the worst case,  $k = \Theta(n)$ .

Triplet probing computes a probe profile for each  $u \in \mathcal{C}$  by evaluating all unordered pairs  $\{v, w\} \subseteq \{0, \dots, n-1\} \setminus \{u\}$ , i.e.,

$$\binom{n-1}{2} = \Theta(n^2)$$

probes per  $u$ . Therefore, the number of probe evaluations per round is  $\Theta(kn^2) = \Theta(n^3)$ .

Each probe evaluation constructs a temporary augmented graph and recomputes: (i) a spectral decomposition and (ii) the induced original-only signature partition. Both are computed on a graph whose size is  $N$ , hence the per-probe cost is  $O(N^3)$  in the dense eigendecomposition model. Therefore, the worst-case time for triplet probing in a single refinement round is

$$\Theta(n^3) \cdot O(N^3) = O(n^3 N^3).$$

## 7.5 Worst-case number of rounds

We assume at most  $n$  permanent individualization steps. Each refinement round performs at least one permanent attachment (either one matched representative pair or multiple matched singleton pairs), hence the total number of refinement rounds is at most  $R = O(n)$ .

## 7.6 Total worst-case time bound

Combining the above:

- per round worst-case cost is dominated by triplet probing:  $O(n^3 N^3)$ ,

- number of rounds is  $O(n)$ ,
- and in the worst case  $N = \Theta(n^2)$  due to the cumulative clique growth (even if the original graph is sparse).

Thus the total worst-case time is

$$O(n \cdot n^3 N^3) = O(n^4 N^3).$$

Substituting  $N = \Theta(n^2)$  gives the explicit worst-case bound  $O(n^{10})$ . This is a conservative worst-case bound under the assumptions stated at the beginning of the section.

## 7.7 Worst-case space bound

The dominant memory cost in any stage arises from storing dense spectral objects for the working graph: the Laplacian (or an equivalent dense representation) and the eigenvector matrix. This requires  $O(N^2)$  space per graph, hence still  $O(N^2)$  overall up to constants. In the worst case  $N = \Theta(n^2)$ , therefore the worst-case space usage is  $O(n^4)$ .

Temporary probe graphs do not asymptotically increase peak memory beyond  $O(N^2)$  because they can be constructed and discarded per probe evaluation; peak usage remains dominated by the spectral matrices.

## 7.8 Verification cost

When a candidate bijection is constructed, explicit verification checks adjacency preservation on the original graphs. This requires  $O(m)$  time (or  $O(n^2)$  in dense representation) and  $O(1)$  additional working memory beyond the input storage, and thus does not affect the asymptotic worst-case bounds above.

# 8 Implementation details

This section records implementation-level decisions that ensure determinism, numerical stability, and reproducibility. Only aspects not already covered in the algorithmic description are discussed here.

## Subdivision policy

Subdivision depth is determined once during initialization. The smallest subdivision level satisfying prescribed vertex-count bounds and non-degenerate spectral-dimension estimation is selected. Subdivision is applied symmetrically and is not increased later.

## Spectral evaluation parameters

Each refinement round computes:

- the combinatorial Laplacian,
- a full eigendecomposition,
- a spectral-dimension estimate,

- short-time curvature coefficients on an iteratively updated time interval

The number of time samples, coefficient depth, and regression parameters are controlled by fixed global constants. These values remain unchanged throughout execution.

### Coefficient quantization

Curvature coefficients are floating-point values derived from spectral computations. They are discretized using deterministic scale-based rounding.

For a coefficient value  $x$ :

1. Non-finite values (NaN or  $\pm\infty$ ) are mapped to 0.
2. The value is multiplied by a fixed scaling constant.
3. The result is rounded to the nearest integer.
4. It is then rescaled back to floating point.
5. Optionally, the value may be snapped to a fixed bucket size.
6. Values whose magnitude falls below a fixed threshold are clamped to zero.

All constants governing scale, bucket size, and thresholding are fixed globally. The same discretization is applied to both graphs. This procedure prevents spurious refinement caused by insignificant floating-point perturbations.

### Floating-point tolerance in spectral grouping

During construction of the curvature time grid, near-equal spectral quantities are merged using a tolerance that is bounded below by the local floating-point unit-in-the-last-place (ULP). This prevents instability when eigenvalues are extremely close. ULP-based tolerance is used only in this spectral grouping step, not in curvature coefficient quantization.

### Signature construction

BFS-curvature signatures are constructed exclusively for original vertices. Auxiliary gadget vertices influence signatures only through graph structure; they are never assigned signature identities.

Signature keys consist of:

- discretized curvature coefficient vectors,
- BFS-layer aggregation summaries,
- structural counts derived deterministically from the graph.

All signature components are deterministically ordered.

## Probing configuration

When a smallest unresolved matched class is selected:

- Pair probing evaluates all ordered pairs  $(u, v)$  with  $u$  in the selected class and  $v$  any other original vertex.
- Two symmetric gadget orientations are evaluated.
- Probe profiles are constructed as frequency maps of canonicalized outcome keys.
- If pair probing yields a single refined group in both graphs, triplet probing is invoked.

Probe configurations are enumerated in lexicographic vertex order. No heuristic prioritization or adaptive search is used.

## Permanent individualization

If probing does not produce complete separation, a permanent clique of size  $q$  is attached to matched vertices. The parameter  $q$  begins at a fixed constant and increases by one after each attachment. We start with  $q = 3$  (since subdivision guarantees that our graphs contain no cliques of size greater than two). Each clique introduces fresh vertices. Because  $q$  increases monotonically, later attachments are structurally distinguishable from earlier ones.

## Twin detection

Twin classes are detected directly on the original graphs. For each non-singleton class:

- true twins are verified by mutual adjacency and identical external neighborhoods,
- false twins are verified by non-adjacency and identical external neighborhoods.

If corresponding twin classes match in both graphs, a canonical bijection is constructed by deterministic ordering within each class. The bijection is then explicitly verified.

## Determinism and reproducibility

All constants controlling:

- subdivision bounds,
- spectral coefficient depth,
- time-grid construction,
- quantization scale and bucket size,
- probing gadget sizes,

are fixed in advance. No randomness is used. All vertex selections, probe enumerations, class selections, and attachment orders are performed in deterministic index order. Given identical inputs, the implementation produces identical refinement sequences and identical outcomes.

## 9 Experimental results

### 9.1 Randomly generated instances

We begin with a representative positive instance consisting of two graphs  $\mathcal{G}_1$  and  $\mathcal{G}_2$  on  $n = 50$  vertices, where  $\mathcal{G}_2$  is obtained from  $\mathcal{G}_1$  by relabeling a subset of vertices (in this example, 9 vertices are moved to different indices). Figure 2 shows the cumulative eigenvalue counting function  $\rho(\lambda' < \lambda)$  used to estimate the spectral dimension  $d_s$  on a logarithmic scale. We then compute the leading curvature-like coefficient  $u_1(v)$  for every vertex  $v$  in both graphs. Although  $\mathcal{G}_1$  and  $\mathcal{G}_2$  are isomorphic, the vertex ordering differs, and therefore the sequences  $\{u_1(v)\}_{v \in V(\mathcal{G}_1)}$  and  $\{u_1(v)\}_{v \in V(\mathcal{G}_2)}$  need not match entry-wise; this mismatch is highlighted in Figure 3.

To infer a correspondence, we form the pairwise difference matrix

$$C_{ij} = \log|u_1(v_i \in V(\mathcal{G}_1)) - u_1(w_j \in V(\mathcal{G}_2))|,$$

shown in Figure 4. Flattening and sorting the entries of  $C$  yields a one-dimensional list in which a pronounced gap separates near-matching curvature pairs from the remaining pairs. We detect the largest gap to obtain the threshold  $C_{\text{critical}}$  and examine the cumulative count  $S(C)$ ; Figure 5(a) shows that the number of pairs below  $C_{\text{critical}}$  equals  $n$  for this instance, consistent with isomorphism. A vertex pairing is then obtained by sorting vertices by their curvature-derived values and matching ranks, as illustrated in Figure 5(b). Finally, as in all experiments, any proposed correspondence is explicitly verified to preserve adjacency on the original graphs.

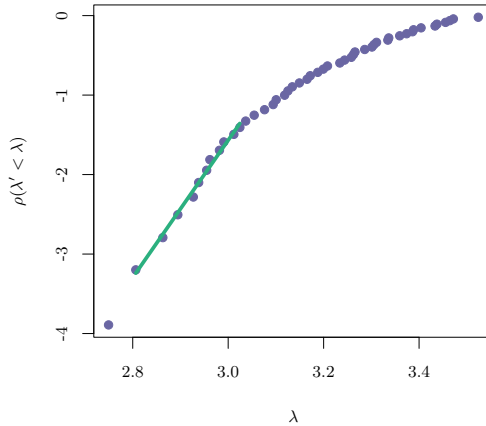


Figure 2: The spectral dimension  $d_s = 17$  recovered for  $\mathcal{G}_1$  with  $n = 50$ .

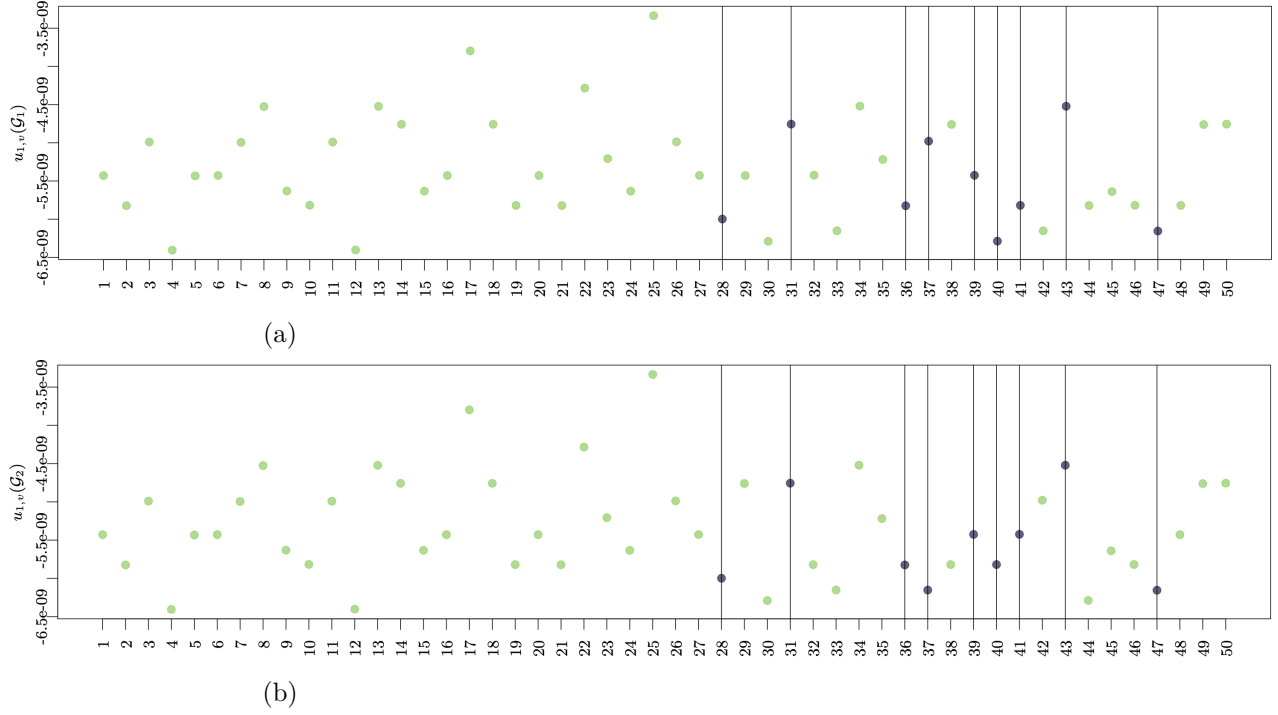


Figure 3: The curvature-derived values  $u_1(v)$  for  $\mathcal{G}_1$  and  $\mathcal{G}_2$ . The vertical lines indicate indices of labeled vertices.

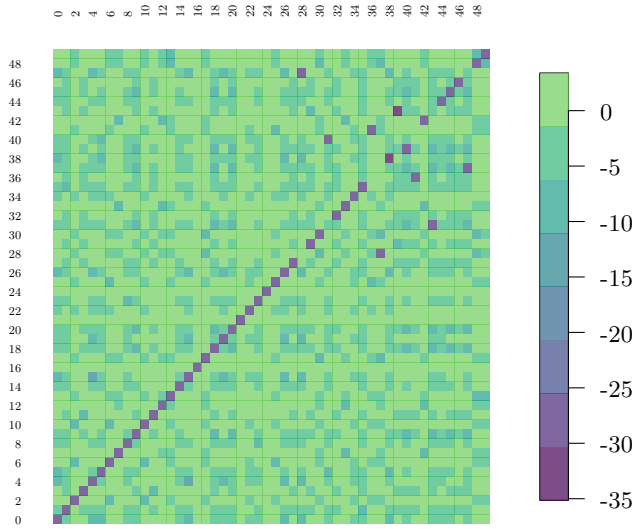


Figure 4: Heatmap of  $C_{ij}$  for the isomorphic pair. The 9 labeled vertices appear as off-diagonal structure.

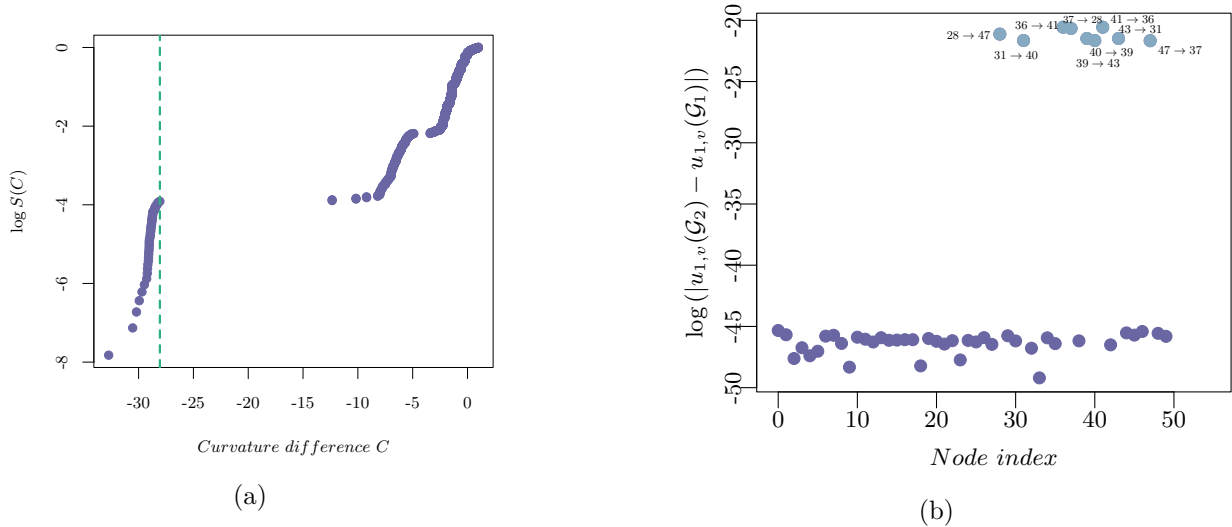


Figure 5: (a) The number of pairs below the dashed vertical line (denoting  $C_{\text{critical}}$ ) equals  $n$ , consistent with isomorphism. (b) The induced rank-based pairing from sorted curvature-derived values.

We also evaluate negative instances in which the two graphs are non-isomorphic. As an illustrative example, we consider two graphs that differ by a single edge switch. Figure 6(a) shows the corresponding sorted curvature-difference behavior. In contrast to the isomorphic case, the curve  $\log(S(C))$  does not exhibit a clear separation into  $n$  near-matching pairs; correspondingly, the number of pairs below the first prominent gap is  $\ll n$ , and the graphs are declared non-isomorphic. Figure 6(b) shows the heatmap of pairwise curvature differences for this case.

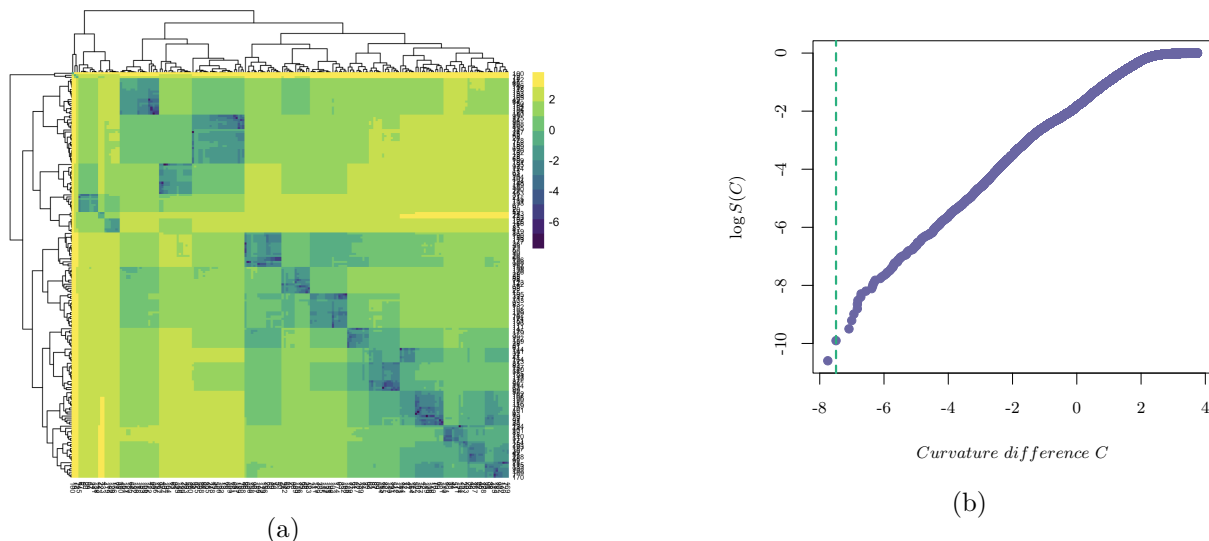


Figure 6: Two graphs  $\mathcal{G}_1$  and  $\mathcal{G}_2$  are one edge-switch away from isomorphism. (a) The number of pairs below the first gap in  $C_{\text{critical}}$  is not  $n$ , and the graphs are declared non-isomorphic. (b) Heatmap of the pairwise difference  $|u_1(v_i) - u_1(w_j)|$  for random graphs with  $n = 200$  and non-homogeneous degree.

We further carry out the computation across nine graph families, generating five instances per family. Our framework succeeded on all instances tested; for brevity, we show one representative pair from each class below.

### 9.1.1 Random geometric graphs

We apply our framework to random geometric graphs on  $n = 500$  vertices with non-homogeneous degree distributions. The eigenvalue counting function  $\rho$ , the degree distribution, and the heatmap of  $C$  are shown in Figure 7.

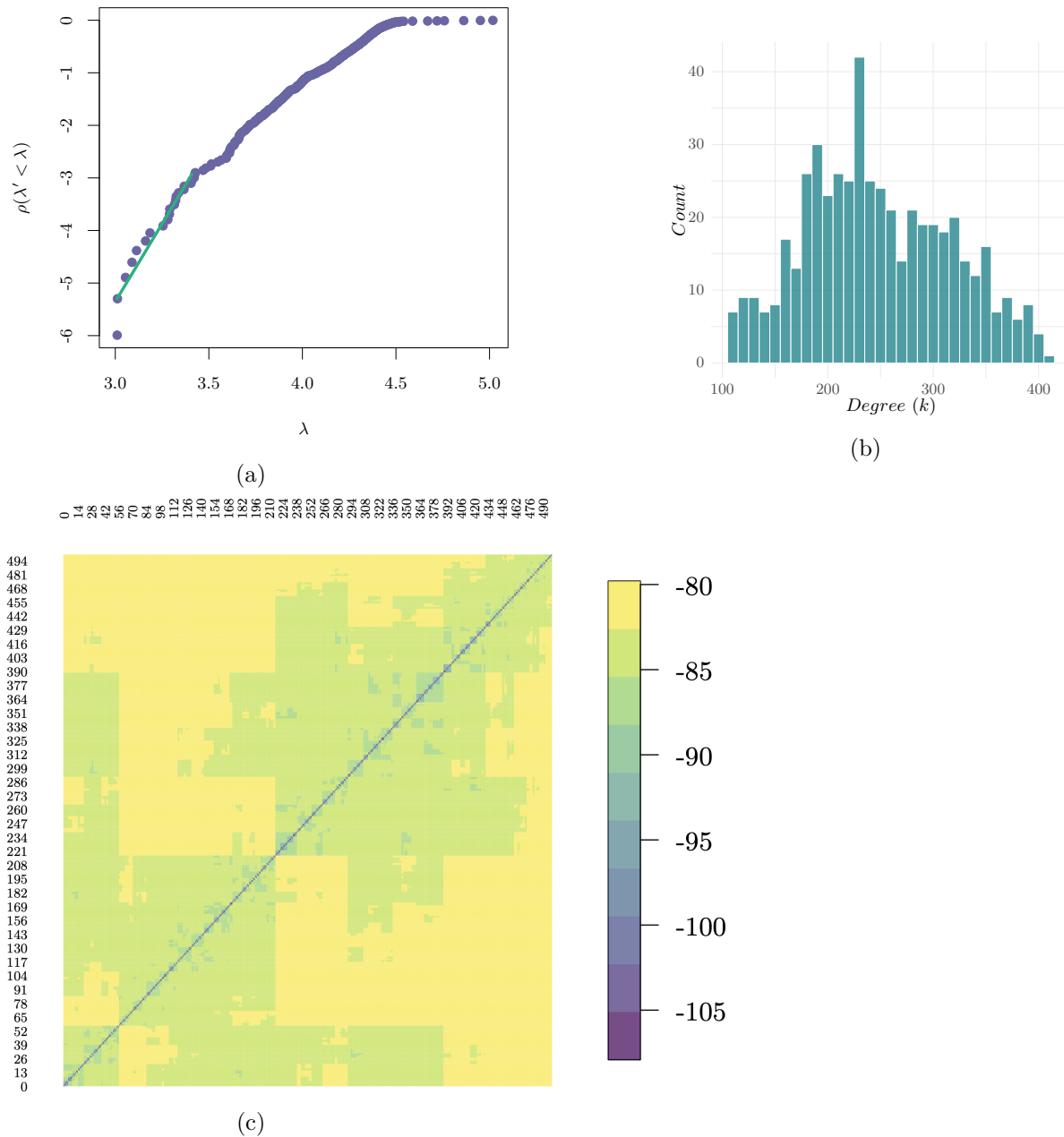


Figure 7: Recovered spectral dimension  $d_s = 30.32$ , degree distribution of  $\mathcal{G}_1$ , and heatmap of the pairwise logarithmic difference  $\log |u_1(v_i) - u_1(w_j)|$  for random geometric graphs with  $n = 500$ .

### 9.1.2 Power-law cluster graphs

We apply our framework to power-law cluster graphs on  $n = 500$  vertices with non-homogeneous degree distributions. The eigenvalue counting function  $\rho$ , the degree distribution, and the heatmap of  $C$  are shown in Figure 8.

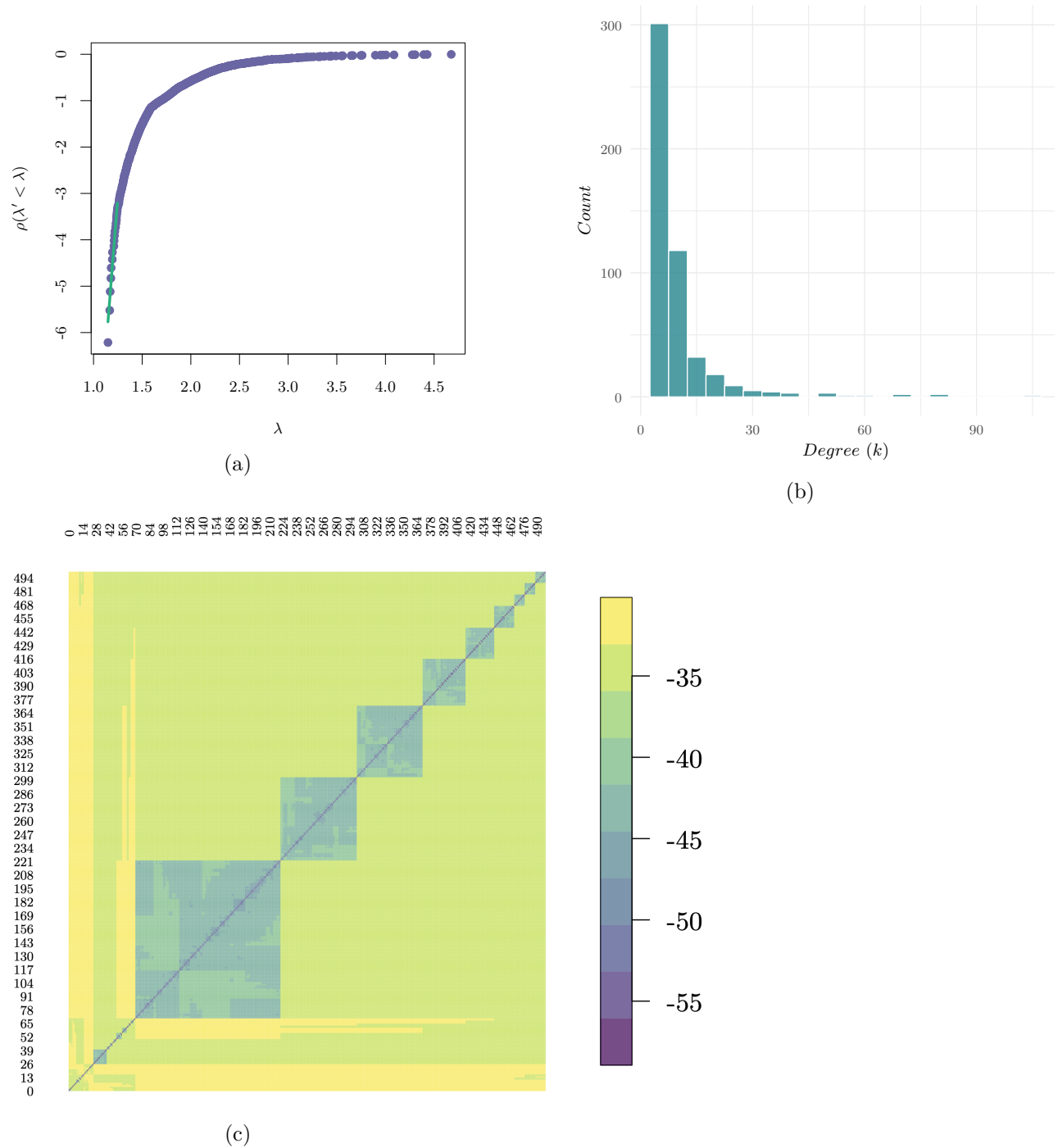


Figure 8: Recovered spectral dimension  $d_s = 46.89$ , degree distribution of  $\mathcal{G}_1$ , and heatmap of the pairwise logarithmic difference  $\log |u_1(v_i) - u_1(w_j)|$  for power-law cluster graphs with  $n = 500$ .

### 9.1.3 Stochastic block graphs

We apply our framework to stochastic block graphs on  $n = 500$  vertices with non-homogeneous degree distributions. The eigenvalue counting function  $\rho$ , the degree distribution, and the heatmap of  $C$  are shown in Figure 9.

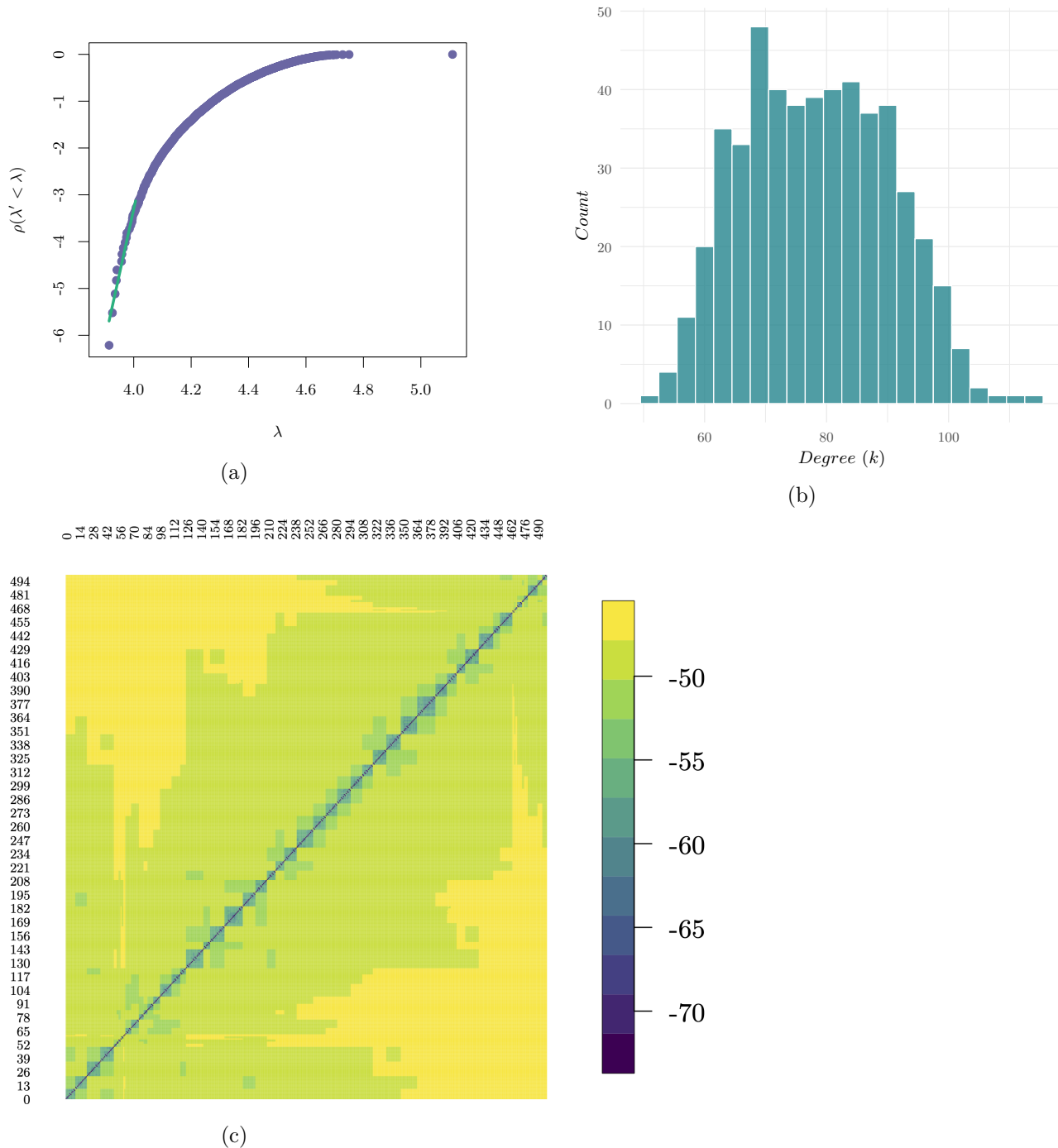


Figure 9: Recovered spectral dimension  $d_s = 49$ , degree distribution of  $\mathcal{G}_1$ , and heatmap of the pairwise logarithmic difference  $\log |u_1(v_i) - u_1(w_j)|$  for stochastic block graphs with  $n = 500$ , with inter-community probability  $p_{\text{inter}} = 0.1$  and intra-community probability  $p_{\text{intra}} = 0.25$ .

### 9.1.4 Regular graphs

We apply our framework to regular graphs on  $n = 500$  vertices. The eigenvalue counting function  $\rho$  and the heatmap of  $C$  are shown in Figure 10.

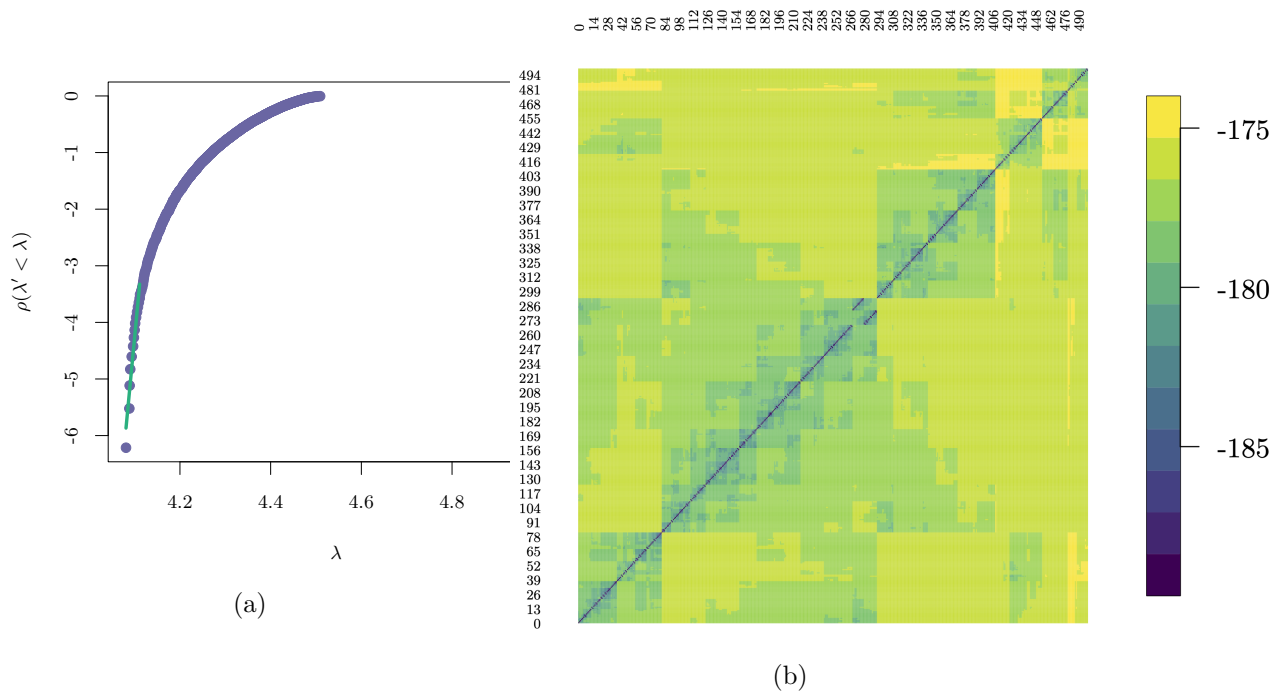


Figure 10: Recovered spectral dimension  $d_s = 146.06$  and heatmap of the pairwise logarithmic difference  $\log |u_1(v_i) - u_1(w_j)|$  for regular graphs with  $n = 500$  and homogeneous degree  $k = 10$ .

### 9.1.5 Albert–Barabási graphs

We apply our framework to Albert–Barabási graphs on  $n = 500$  vertices with non-homogeneous degree distributions. The eigenvalue counting function  $\rho$ , the degree distribution, and the heatmap of  $C$  are shown in Figure 11.

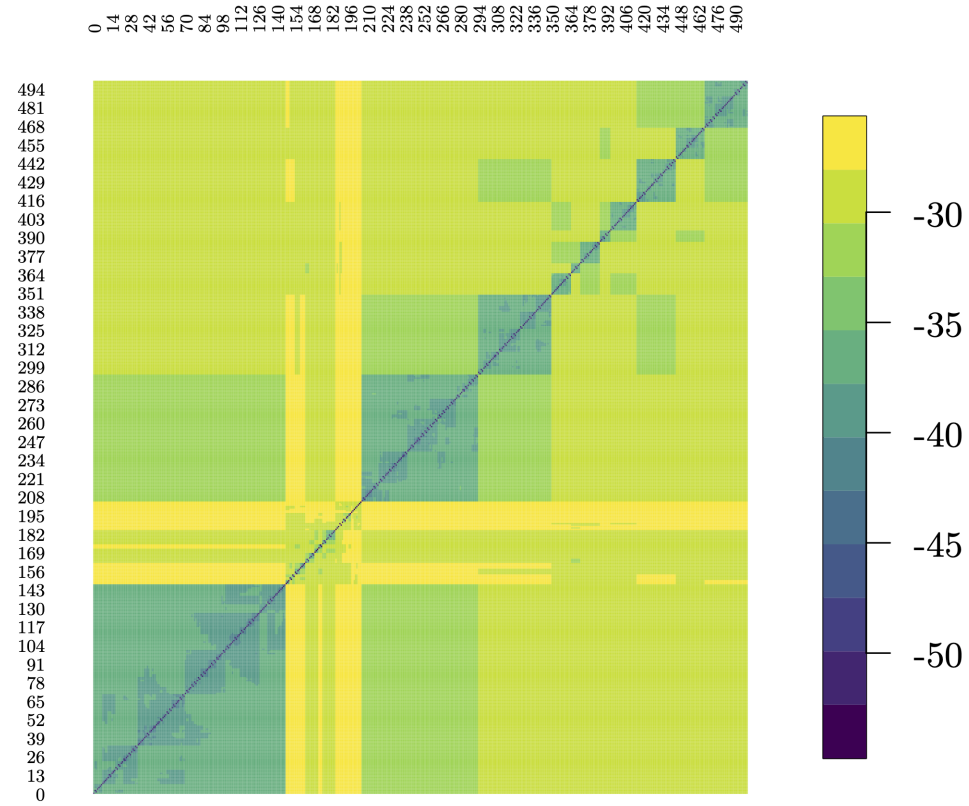
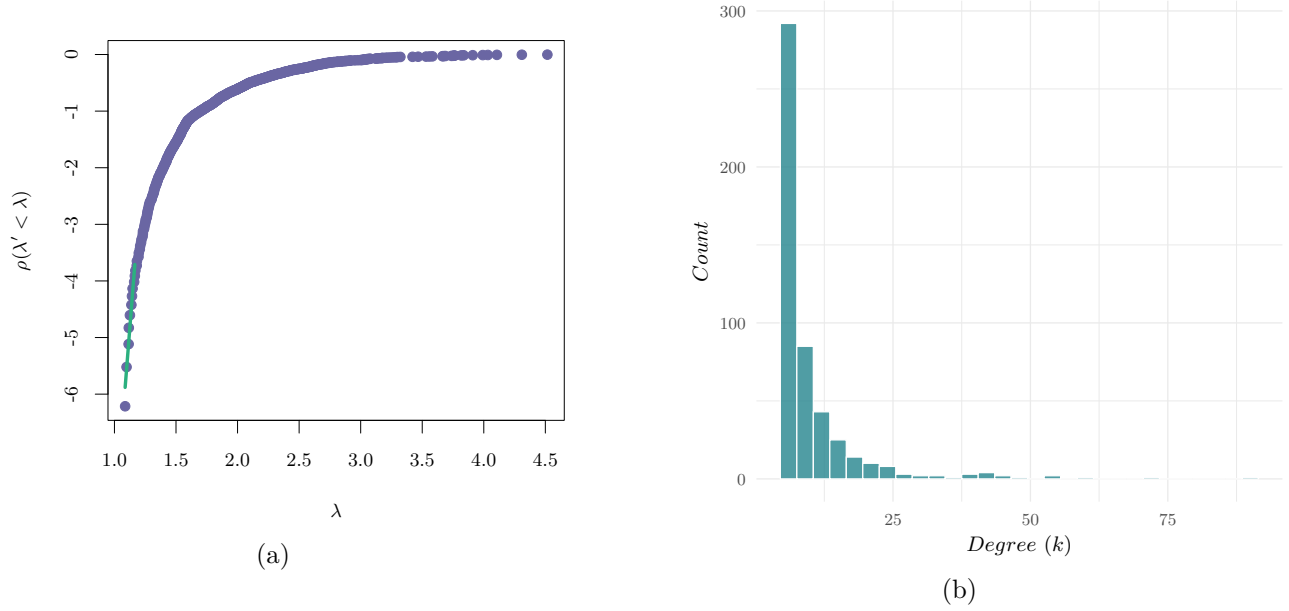


Figure 11: Recovered spectral dimension  $d_s = 45.70$ , degree distribution of  $\mathcal{G}_1$ , and heatmap of the pairwise logarithmic difference  $\log |u_1(v_i) - u_1(w_j)|$  for Albert–Barabási graphs with  $n = 500$ , and power-law coefficient of 2.72.

### 9.1.6 Watts–Strogatz graphs

We apply our framework to Watts–Strogatz graphs on  $n = 500$  vertices with non-homogeneous degree distributions. The eigenvalue counting function  $\rho$ , the degree distribution, and the heatmap of  $C$  are shown in Figure 12.

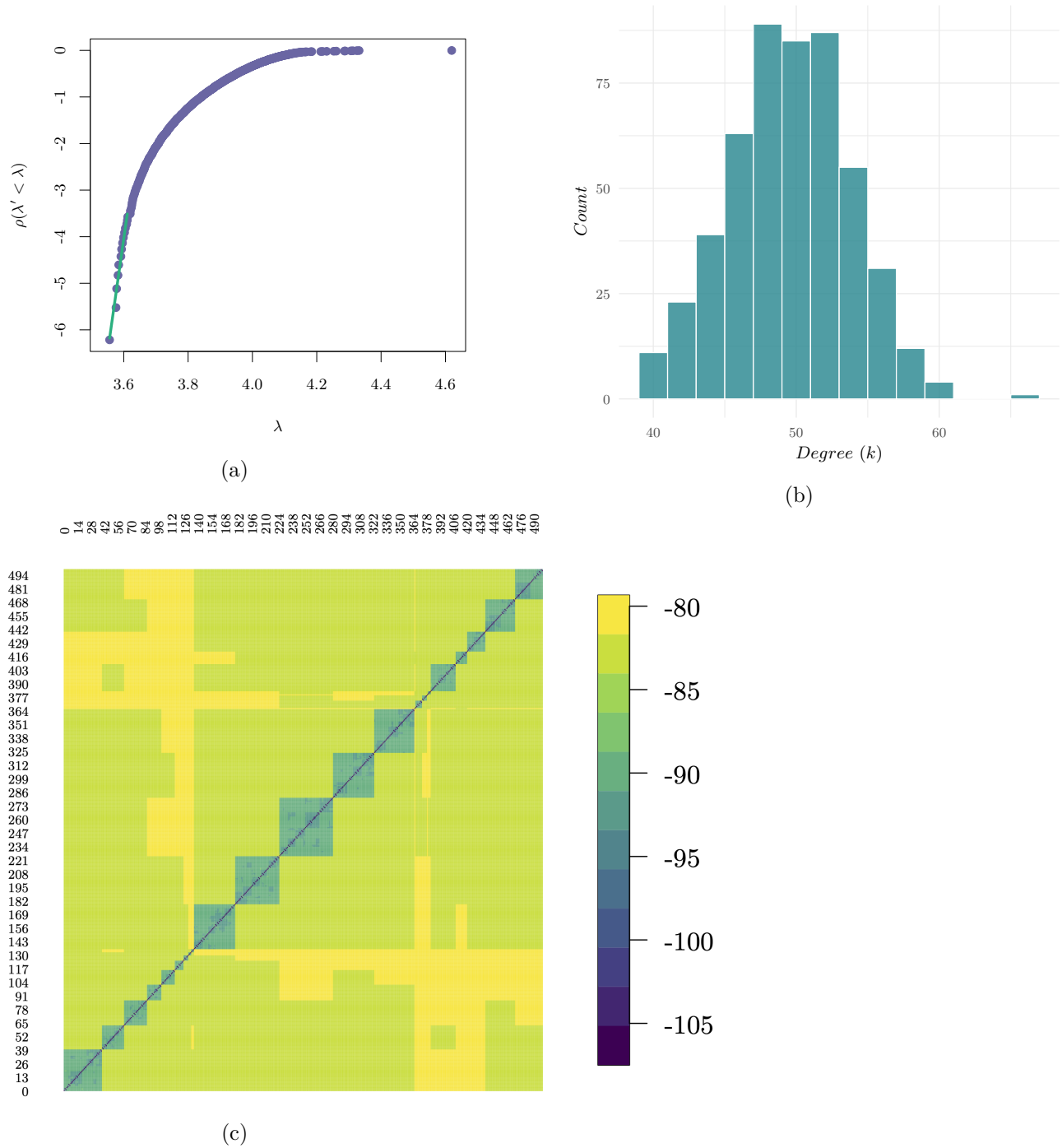


Figure 12: Recovered spectral dimension  $d_s = 93.13$ , degree distribution of  $\mathcal{G}_1$ , and heatmap of the pairwise logarithmic difference  $\log |u_1(v_i) - u_1(w_j)|$  for Watts–Strogatz graphs with  $n = 500$ , mean degree  $k_{\text{mean}} = 50$ , and rewiring probability 0.5.

### 9.1.7 Erdős–Rényi graphs

We apply our framework to Erdős–Rényi graphs on  $n = 500$  vertices with non-homogeneous degree distributions. The eigenvalue counting function  $\rho$ , the degree distribution, and the heatmap of  $C$  are shown in Figure 13.

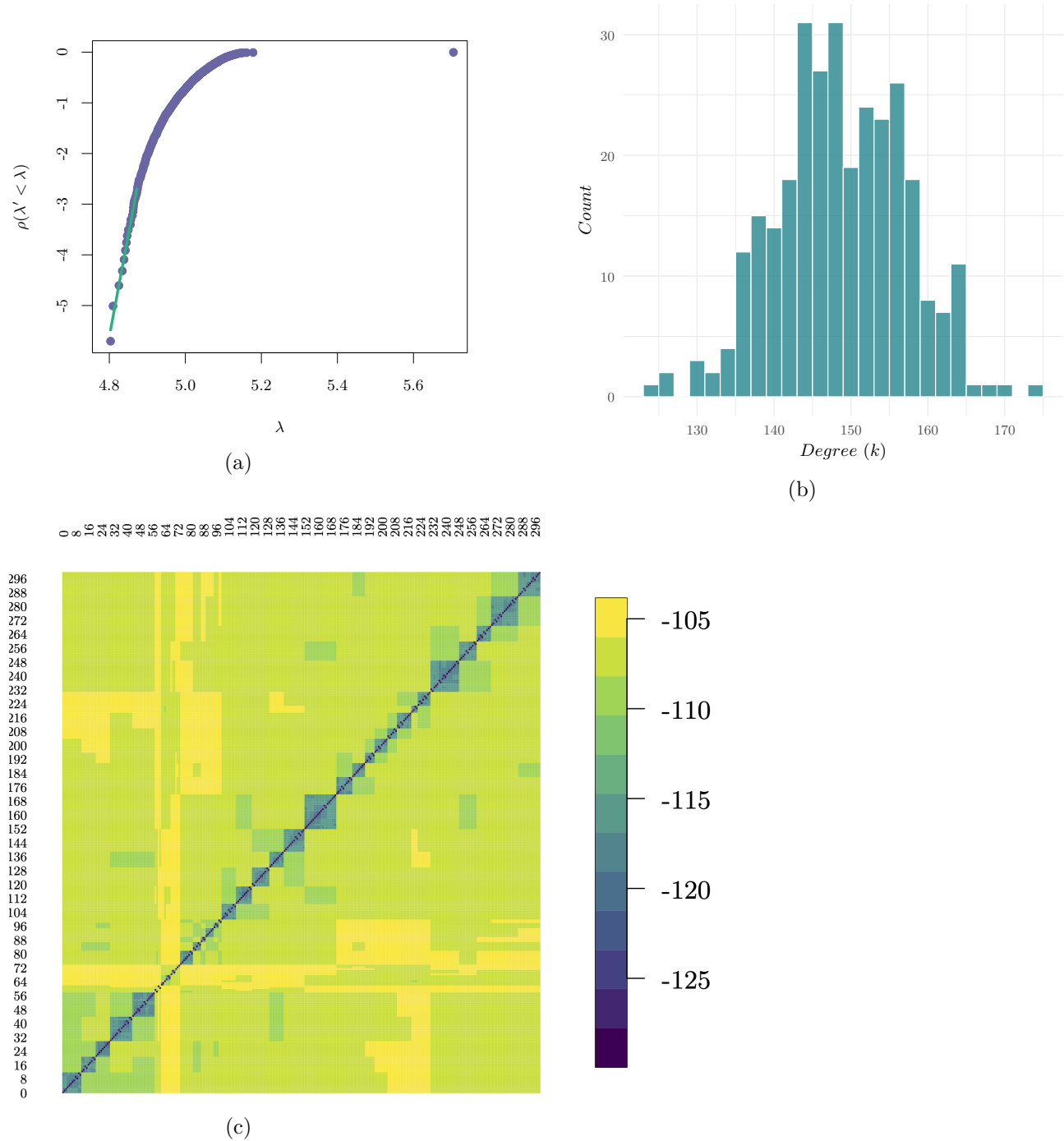


Figure 13: Recovered spectral dimension  $d_s = 75.78$ , degree distribution of  $\mathcal{G}_1$ , and heatmap of the pairwise logarithmic difference  $\log |u_1(v_i) - u_1(w_j)|$  for Erdős–Rényi graphs with  $n = 500$  and an edge probability of 0.5.

### 9.1.8 Tree graphs

We apply our framework to tree graphs on  $n = 500$  vertices. The eigenvalue counting function  $\rho$ , the degree distribution, and the heatmap of  $C$  are shown in Figure 14.

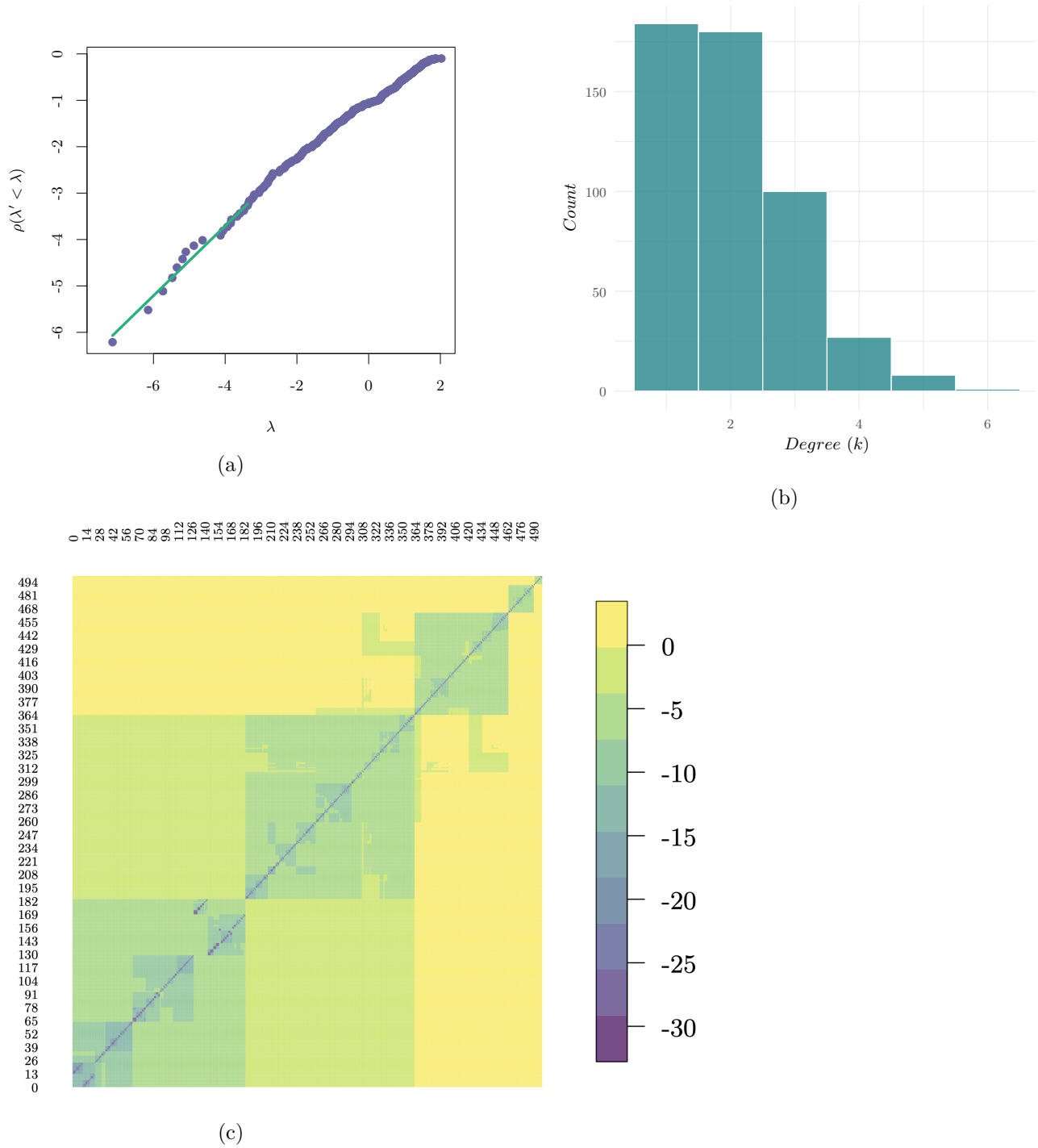


Figure 14: Recovered spectral dimension  $d_s = 1.45$ , degree distribution of  $\mathcal{G}_1$ , and heatmap of the pairwise logarithmic difference  $\log |u_1(v_i) - u_1(w_j)|$  for trees with  $n = 500$ .

### 9.1.9 Paley graphs

We apply our framework to Paley graphs, for which we show the non-subdivided and subdivided versions in Figure 15. We start by evaluating curvature on the subdivided graphs shown in Figure 16. They exhibit total symmetry in curvature among the original vertices, on the one hand, and the subdivision vertices on the other (not all subdivision vertices share similar curvature but those differences are not visually detectable).

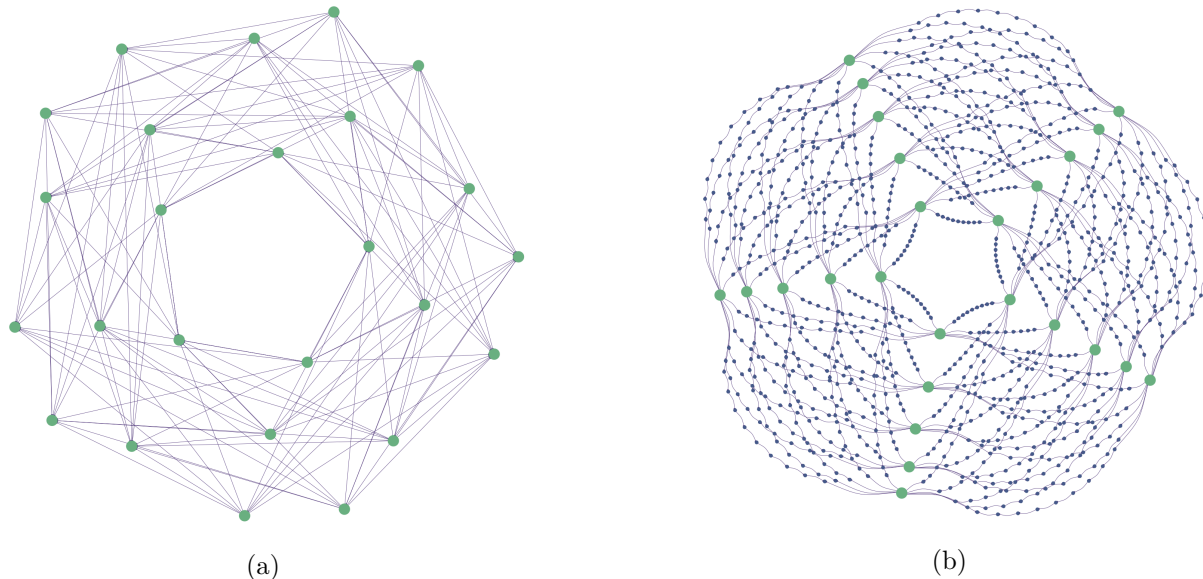


Figure 15: (a) The original Paley graph. (b) The subdivided version that ensures a power-law behavior of the eigenvalue density  $\rho(\lambda' < \lambda)$ .

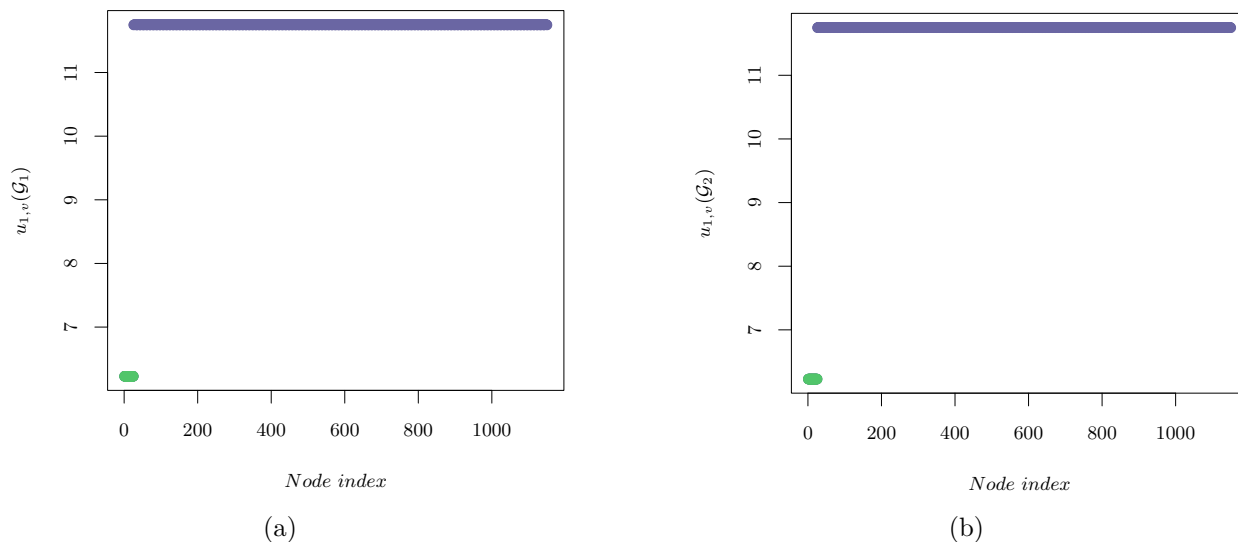


Figure 16: Curvatures  $u_1(v)$  for the subdivided Paley graphs, showing symmetry among the original vertices and among the auxiliary vertices (cf. Figure 15(b)).

We show the results of the symmetry breaking construction for vertex individualization in Figure 17. We then compute curvatures associated with the resultant graphs shown in Figure 18. They exhibit a clear breaking of symmetry allowing us to identify an isomorphic mapping between vertices using sorted curvature values.

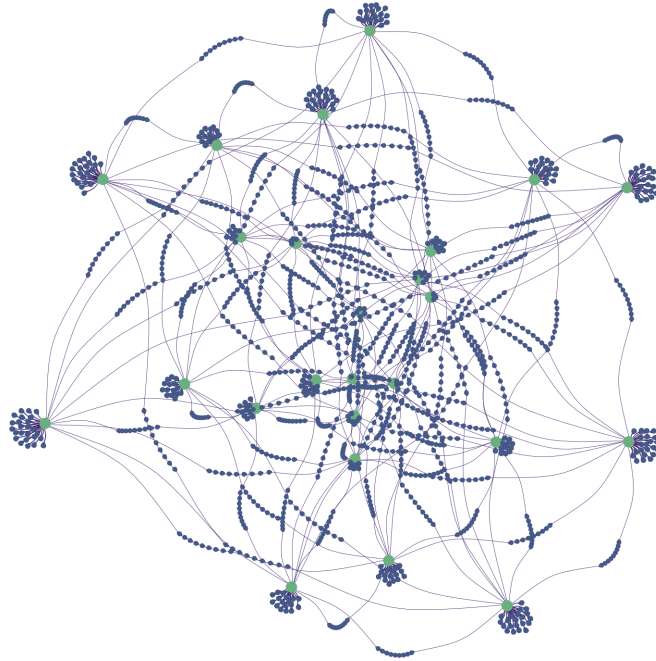


Figure 17: The resulting graph of the symmetry breaking construction for vertex identification/individualization.

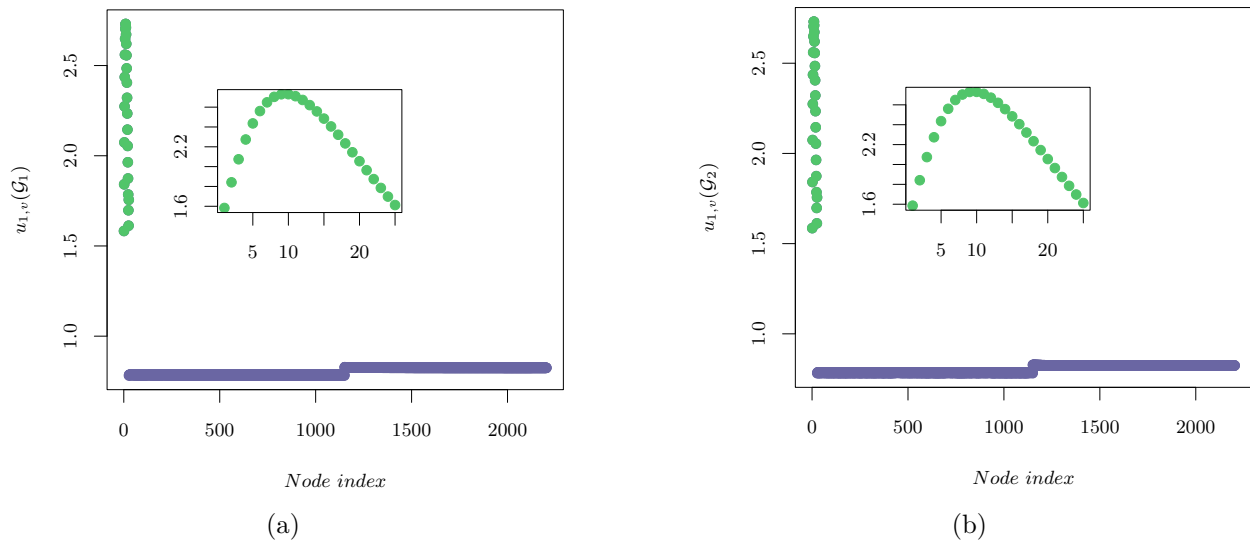


Figure 18: Curvatures  $u_1(v)$  for the Paley graphs after applying the vertex identification/individualization algorithm, which breaks the symmetry and enables recovery of an isomorphic correspondence via sorted curvature values.

## 9.2 Known benchmark graphs

We evaluate the algorithm on curated benchmark instances drawn from the repository hosted at <https://pallini.di.uniroma1.it/Graphs.html>. These graphs include many classical stress tests for refinement- and spectrum-based isomorphism procedures (e.g., highly regular families, strongly regular constructions, cages, and projective or algebraic graphs). The purpose of this section is to complement the randomly generated experiments of the previous section with standardized, named instances that are widely used in the literature.

Each family’s files in the repository follow a naming pattern: for example, `ag_*`, `cfi_*`, `grid_*`, `latin_*`, etc., typically with the family code as prefix. More broadly, limitations of WL-style refinement and related GI discussion appear in [36, 13]. Due to running time and memory-usage constraints, we consider only benchmark graphs from the repository with at most 250 original vertices (400 for some of the “easier” classes) and at most 1000 vertices after subdivision.

### 9.2.1 Experimental protocol

**Isomorphic-only evaluation.** Our benchmark evaluation focuses on isomorphic instances. For each input graph  $G$  we generate  $R = 3$  relabeled copies  $G^{(r)} = \pi_r(G)$  using deterministic permutations  $\pi_r$  derived from a fixed global seed. Each trial therefore consists of a pair  $(G, G^{(r)})$  that is guaranteed to be isomorphic.

**Success criterion and one-sided correctness.** A run is counted as successful only if the algorithm outputs an explicit bijection  $f : V(G) \rightarrow V(G^{(r)})$  on the original vertices and the mapping is verified by direct adjacency preservation on the unmodified input graphs. Because we only accept mappings that pass this final check, the method is one-sidedly correct: it does not produce false positive isomorphisms.

**Staged solver configuration (pairs  $\rightarrow$  triplets  $\rightarrow$  precision).** Each isomorphic trial is attempted under an escalation schedule reflecting the solver design. We first run the refinement and augmentation pipeline using pair probing only (triplet probes disabled). If the run fails, we re-run the same trial with triplet probing enabled as a fallback. If the trial still fails, we re-run with more conservative numerical settings to mitigate spectral/curvature quantization instability by controlling eigenvalue scaling, spectral-dimension stability thresholds, and curvature-coefficient scaling, respectively.

### 9.2.2 Affine geometry graphs

Affine geometry graphs arise from finite affine geometries (e.g. points of  $AG(n, q)$ ) and are highly regular. They are typically constructed by taking the points of an affine space over  $\mathbb{F}_q$  and adding edges according to linear relations or distances in that geometry. The result is often a strongly regular or distance-regular graph with a large automorphism group (induced by the affine group). Such symmetry makes them challenging for isomorphism tools, as many vertices are combinatorially indistinguishable. In the repository these graphs have filenames beginning with `ag`. The spectrum typically has few distinct eigenvalues (due to the high symmetry), reflecting its regular structure. Table 1 lists all graphs that were successfully solved. A sample graph is shown in Figure 19.

Graph Name	Original		# Subdivisions	After Subdivision		Triplet Probing Enabled
	$n$	$m$		$N$	$M$	
ag2-02	10	12	4	58	60	No
ag2-03	21	36	1	57	72	No
ag2-04	36	80	1	116	160	No
ag2-05	55	150	1	205	300	Yes
ag2-07	105	392	1	497	784	Yes

Table 1: Original graph parameters  $(n, m)$  and resulting parameters  $(N, M)$  after edge subdivision.

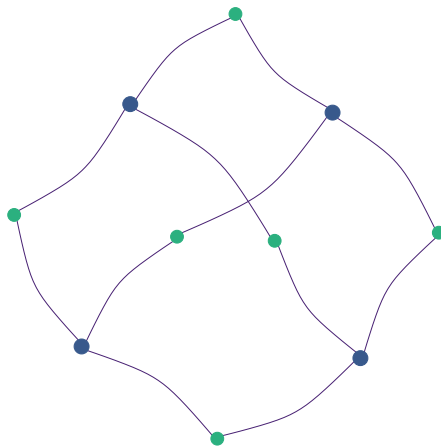


Figure 19: Graph ag2-02 is shown and the vertices are color coded by degree. It has  $n = 10$  vertices with degrees 2 and 3.

### 9.2.3 Cai-Fürer-Immerman graphs

This canonical family is built using the CFI construction and is designed to defeat low-dimensional refinement procedures in the Weisfeiler–Leman (WL) hierarchy. In practice these instances are difficult for purely local refinement rules and require deeper global reasoning; see, e.g., discussions of refinement limits and WL-type methods in [36, 16, 13]. Filenames in the repository start with `cfi`. Table 2 lists all graphs that were successfully solved, with a sample graph shown in Figure 20.

Graph Name	Original		# Subdivisions	After Subdivision		Triplet Probing Enabled
	$n$	$m$		$N$	$M$	
cfi-20	200	300	0	200	300	No
cfi-22	220	330	0	220	330	No
cfi-24	240	360	0	240	360	No
cfi-26	260	390	0	260	390	No
cfi-28	280	420	0	280	420	No
cfi-30	300	450	0	300	450	No

Table 2: Original graph parameters  $(n, m)$  and resulting parameters  $(N, M)$  after edge subdivision.

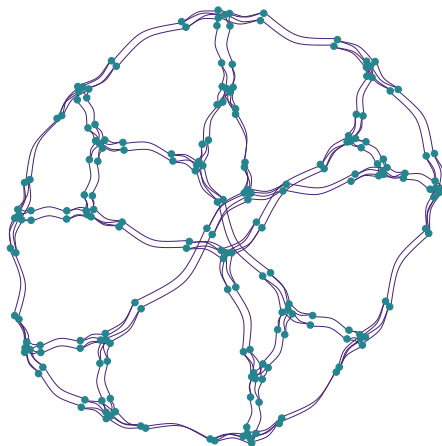


Figure 20: Graph cfi-20 is shown, with  $n = 200$  and a homogenous degree of 3.

### 9.2.4 Miyazaki graphs

Miyazaki graphs are hard, parameterized graphs from Miyazaki-style constructions. They are used as stress tests because they are very regular and can require considering large-scale swaps to distinguish variants. The repository uses filenames with `cmz` or `mz` (and `mz-aug`, `mz-aug2` for augmented versions). Table 3 lists all graphs that were successfully solved. A sample graph is shown in Figure 21.

Graph Name	Original		# Subdivisions	After Subdivision		Triplet Probing Enabled
	$n$	$m$		$N$	$M$	
cmz-5	120	190	0	120	190	No
cmz-6	144	228	0	144	228	No
cmz-7	168	266	0	168	266	No
cmz-8	192	304	0	192	304	No
cmz-9	216	342	0	216	342	No
cmz-10	240	380	0	240	380	No
mz-2	40	60	1	100	120	No
mz-4	80	120	0	80	120	No
mz-6	120	180	0	120	180	No
mz-8	160	240	0	160	240	No
mz-10	200	300	0	200	300	No
mz-aug-2	40	92	1	132	184	No
mz-aug-4	80	184	0	80	184	No
mz-aug-6	120	276	0	120	276	No
mz-aug-8	160	368	0	160	368	No
mz-aug2-4	96	152	0	96	152	No
mz-aug2-6	144	228	0	144	228	No
mz-aug2-8	192	304	0	192	304	No
mz-aug2-10	240	380	0	240	380	No

Table 3: Original graph parameters  $(n, m)$  and resulting parameters  $(N, M)$  after edge subdivision.

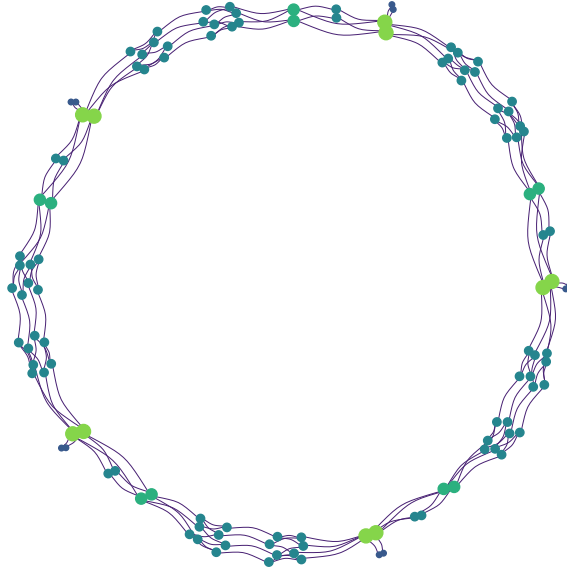


Figure 21: Graph cmz-05 is shown, with  $n = 120$  vertices, color coded by degree 2, 3, 4, and 5.

### 9.2.5 Grid graphs

The (Cartesian) grid graphs are formed as the product of two path graphs. A typical grid graph on  $m \times n$  vertices connects each vertex to its neighbors in a square lattice. They are planar, bipartite, and have many automorphisms (translations and reflections). In the repository, file names begin with `grid`. These graphs have simple spectra (being Cartesian products) and are relevant as a baseline. Grid graphs with switched edges (grid-sw) are derived by taking a grid graph and swapping a pair of edges in each of several sub-squares. The operation preserves degree sequences but can obfuscate global structure. The repository files use prefix `grid-sw`. Such switched-edge graphs can be harder for refinement algorithms because local neighborhoods remain similar even though global geometry changes. Table 4 lists all graphs that were successfully solved, and a sample graph is shown in Figure 22.

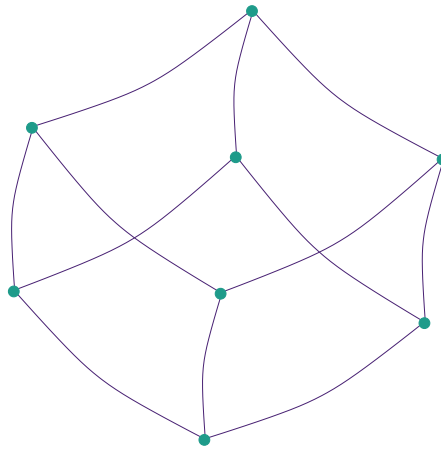


Figure 22: Graph grid-w-3-2 with  $n = 8$ .

Graph Name	Original		# Subdivisions	After Subdivision		Triplet Probing Enabled
	$n$	$m$		$N$	$M$	
grid-2-5	25	40	1	65	80	No
grid-2-10	100	180	0	100	180	No
grid-2-15	225	420	0	225	420	No
grid-2-20	400	760	0	400	760	No
grid-3-2	8	12	4	56	60	No
grid-3-3	27	54	1	81	108	No
grid-3-4	64	144	0	64	144	No
grid-3-5	125	300	0	125	300	No
grid-3-6	216	540	0	216	540	No
grid-3-7	343	882	0	343	882	No
grid-w-2-5	25	50	1	75	100	No
grid-w-2-10	100	200	0	100	200	No
grid-w-2-15	225	450	0	225	450	No
grid-w-2-20	400	800	0	400	800	No
grid-w-3-2	8	12	4	56	60	No
grid-w-3-3	27	81	1	108	162	No
grid-w-3-4	64	192	1	256	384	No
grid-w-3-5	125	375	0	125	375	No
grid-w-3-6	216	648	0	216	648	No
grid-w-3-7	343	1029	0	343	1029	No

Table 4: Original graph parameters  $(n, m)$  and resulting parameters  $(N, M)$  after edge subdivision.

### 9.2.6 Hadamard matrix graphs

Given an  $n \times n$  Hadamard matrix  $H$ , one constructs a Hadamard graph on  $4n$  vertices by introducing row-vertices  $r_i^\pm$  and column-vertices  $c_j^\pm$  and connecting them according to the sign pattern of  $H_{ij}$ . This yields a highly regular bipartite graph; for background and equivalences between Hadamard matrices and associated graphs. Repository files use prefix `had`. One can also apply edge-switching perturbations to Hadamard graphs. These are labeled with `had-sw`. Like other switched-edge families, they remain regular and maintain many local symmetries, so refinement can stall without additional global cues. Table 5 lists all graphs that were successfully solved.

Graph Name	Original		# Subdivisions	After Subdivision		Triplet Probing Enabled
	$n$	$m$		$N$	$M$	
had-1	4	4	12	52	52	No
had-2	8	12	4	56	60	No
had-4	16	40	2	96	120	No
had-8	32	144	1	176	288	No
had-12	48	312	1	360	624	No
had-16	64	544	1	608	1088	No
had-sw-20	80	840	1	920	1680	Yes

Table 5: Original graph parameters  $(n, m)$  and resulting parameters  $(N, M)$  after edge subdivision.

### 9.2.7 Latin square graphs

From a Latin square of order  $n$ , the Latin square graph has  $n^2$  vertices (cells), with adjacency defined by sharing a row, a column, or a symbol. The result is strongly regular and highly symmetric. Filenames start with `latin`. Variants such as `latin-sw` apply controlled edge modifications intended to preserve coarse invariants while changing global structure. Table 6 lists all graphs that were successfully solved.

Graph Name	Original		# Subdivisions	After Subdivision		Triplet Probing Enabled
	$n$	$m$		$N$	$M$	
latin-2	4	6	8	52	54	No
latin-3	9	27	2	63	81	No
latin-4	16	72	2	160	216	No
latin-5	15	150	2	325	450	No
latin-6	36	270	2	576	810	No
latin-7	49	441	2	931	1323	No

Table 6: Original graph parameters  $(n, m)$  and resulting parameters  $(N, M)$  after edge subdivision.

### 9.2.8 Lattice graphs

Lattice graphs are general mesh/product graphs. In the repository (`lattice` files) they refer to regular tiling graphs or Cartesian products in low dimensions. Names begin with `lattice`. Table 7 lists all graphs that were successfully solved.

Graph Name	Original		# Subdivisions	After Subdivision		Triplet Probing Enabled
	$n$	$m$		$N$	$M$	
lattice-4	16	48	2	112	144	No
lattice-5	25	100	2	225	300	No
lattice-6	36	180	2	396	540	No
lattice-7	49	294	2	637	882	No
lattice-8	64	448	2	960	1344	No

Table 7: Original graph parameters  $(n, m)$  and resulting parameters  $(N, M)$  after edge subdivision.

### 9.2.9 Additional Paley graphs

For a prime power  $q \equiv 1 \pmod{4}$ , the Paley graph of order  $q$  has vertex set  $\mathbb{F}_q$  and edges  $\{a, b\}$  whenever  $a - b$  is a quadratic residue in  $\mathbb{F}_q$ . These graphs are classical strongly regular examples and are frequently used as structured benchmarks. Files use prefix `paley`. Table 8 lists all graphs that were successfully solved.

Graph Name	Original		# Subdivisions	After Subdivision		Triplet Probing Enabled
	$n$	$m$		$N$	$M$	
paley-5	5	5	9	50	50	No
paley-9	9	18	3	63	72	No
paley-13	13	39	2	91	117	No
paley-17	17	68	2	153	204	No
paley-25	25	150	2	325	450	No
paley-29	29	203	2	435	609	No
paley-37	37	333	2	703	999	No

Table 8: Original graph parameters  $(n, m)$  and resulting parameters  $(N, M)$  after edge subdivision.

### 9.2.10 Desarguesian projective plane graphs

These are point-line incidence (Levi) graphs of finite projective planes of order  $q$ . They are bipartite regular graphs of degree  $q + 1$  with very uniform local structure and large automorphism groups. Filenames begin with **pg**. Such highly symmetric incidence constructions are representative difficult inputs for isomorphism tools; see, e.g., [15] for invariants and discussion in the GI context. The **pp** family refers to incidence graphs from small projective planes, including non-Desarguesian examples. They have the same coarse parameters as the Desarguesian cases but different combinatorial structure. Filenames begin with **pp**. Table 9 lists all graphs that were successfully solved.

Graph Name	Original		# Subdivisions	After Subdivision		Triplet Probing Enabled
	$n$	$m$		$N$	$M$	
pg2-2	14	21	2	56	63	No
pg2-3	26	52	2	130	156	No
pg2-4	42	105	2	252	315	No
pp-2-1	14	21	2	56	63	No
pp-3-1	26	52	2	130	156	No
pp-4-1	42	105	2	252	315	No

Table 9: Original graph parameters  $(n, m)$  and resulting parameters  $(N, M)$  after edge subdivision.

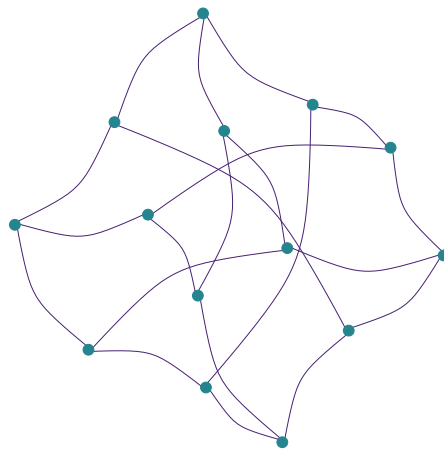


Figure 23: Graph pg2-2 is shown with  $n = 14$  and a homogenous degree of 3.

### 9.2.11 Steiner triple system graphs

From a Steiner triple system, one can form a block-intersection graph: blocks are vertices, and two blocks are adjacent if they share a point. Filenames begin with `sts`, with switched variants `sts-sw` also appearing in some benchmark suites. More broadly, refinement limits and classes where WL-type methods can fail are discussed in [36, 13]. Table 10 lists all graphs that were successfully solved, and a sample representation of the class is shown in Figure 24.

Graph Name	Original		# Subdivisions	After Subdivision		Triplet Probing Enabled
	$n$	$m$		$N$	$M$	
sts-7	7	21	3	70	84	No
sts-9	12	54	2	120	162	No
sts-13	26	195	2	416	585	No
sts-15	35	315	2	665	945	No

Table 10: Original graph parameters  $(n, m)$  and resulting parameters  $(N, M)$  after edge subdivision.

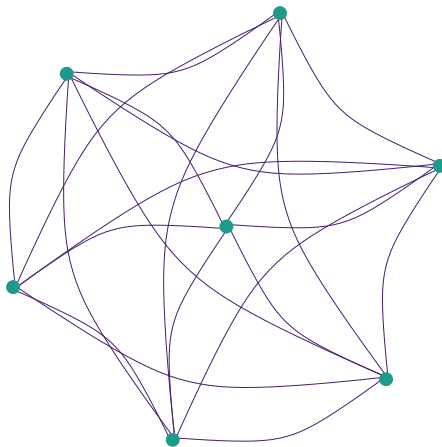


Figure 24: Graph sts-7 with  $n = 7$  is shown with a homogenous degree of 6.

### 9.2.12 Triangular graphs (triang)

The triangular graph  $T_n$  is the line graph of the complete graph  $K_n$ . Its vertices are the  $\binom{n}{2}$  2-subsets of an  $n$ -set, with adjacency given by intersection. In the repository, files are `triang_n`. Table 11 lists all graphs that were successfully solved.

### 9.2.13 Dawar–Yeung graphs (sat\_cfi)

This family (`sat_cfi`) contains SAT-derived gadget graphs that mimic CFI-style hardness characteristics. Filenames are `sat_cfi_*`. Table 12 lists all graphs that were successfully solved. A sample graph is shown in Figure 25.

Graph Name	Original		# Subdivisions	After Subdivision		Triplet Probing Enabled
	$n$	$m$		$N$	$M$	
triang-4	6	12	4	54	60	No
triang-5	10	30	2	70	90	No
triang-6	15	60	2	135	180	No
triang-7	21	105	2	231	315	No
triang-8	28	168	2	364	504	No
triang-9	36	252	2	540	756	No
triang-10	45	360	2	765	1080	No

Table 11: Original graph parameters  $(n, m)$  and resulting parameters  $(N, M)$  after edge subdivision.

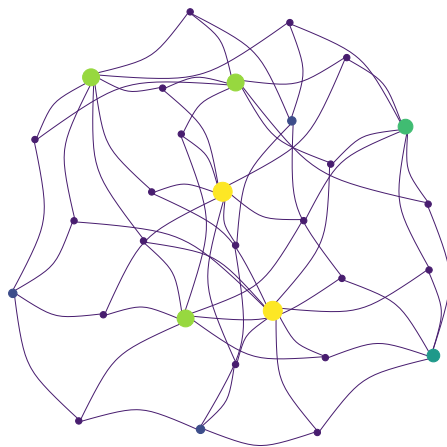


Figure 25: Graph sat-cfi-base-0100-a is shown, with  $n = 30$  vertices, color coded by degree 3, 4, 5, 6, 7, 8.

## 10 Conclusion and future work

We have introduced a deterministic, diffusion-driven framework for graph isomorphism that treats vertex identification as the progressive resolution of multi-scale geometric structure. By extracting curvature-like coefficients from the short-time behavior of the (possibly fractional) graph Laplacian heat kernel and organizing them into BFS-curvature signatures, the algorithm transforms local diffusion data into structured neighborhood-level invariants. These invariants induce a refinement hierarchy that propagates geometric information outward from each vertex in a controlled and canonical manner.

When intrinsic diffusion geometry alone does not fully separate vertices, the refinement process is strengthened through bounded, symmetric mechanisms. These include increasing heat-kernel expansion depth, optional geometric normalization via subdivision to regulate spectral scaling, and structured probing (pair followed by triplet) that exposes higher-order relational asymmetries within unresolved equivalence classes. If refinement stabilizes without achieving termination, deterministic individualization permanently amplifies residual symmetry. All operations are symmetric between the two input graphs and are interpreted exclusively through induced equivalence classes and explicit verification on the original graphs.

Graph Name	Original		# Subd.	After Subdivision		Triplet Probing Enabled
	$n$	$m$		$N$	$M$	
sat_cfi_base_0100_a.dmc	30	60	1	90	120	No
sat_cfi_base_0100_b.dmc	30	60	1	90	120	No
sat_cfi_mult_0100_a.dmc	100	240	0	100	240	No
sat_cfi_mult_0100_b.dmc	100	240	0	100	240	No
sat_cfi_base_0200_a.dmc	60	120	0	60	120	No
sat_cfi_base_0200_b.dmc	60	120	0	60	120	No
sat_cfi_mult_0200_a.dmc	200	480	0	200	480	No
sat_cfi_mult_0200_b.dmc	200	480	0	200	480	No
sat_cfi_base_0300_a.dmc	90	180	0	90	180	No
sat_cfi_base_0300_b.dmc	90	180	0	90	180	No
sat_cfi_base_0400_a.dmc	120	240	0	120	240	No
sat_cfi_base_0400_b.dmc	120	240	0	120	240	No
sat_cfi_base_0500_a.dmc	150	300	0	150	300	No
sat_cfi_base_0500_b.dmc	150	300	0	150	300	No
sat_cfi_base_0600_a.dmc	180	360	0	180	360	No
sat_cfi_base_0600_b.dmc	180	360	0	180	360	No
sat_cfi_base_0700_a.dmc	210	420	0	210	420	No
sat_cfi_base_0700_b.dmc	210	420	0	210	420	No
sat_cfi_base_0800_a.dmc	240	480	0	240	480	No
sat_cfi_base_0800_b.dmc	240	480	0	240	480	No

Table 12: Original graph parameters  $(n, m)$  and resulting parameters  $(N, M)$  after edge subdivision.

The resulting procedure is one-sidedly correct: any bijection returned by the algorithm is explicitly verified and therefore guaranteed to be valid. The overall refinement hierarchy is deterministic and polynomially bounded under dense linear algebra, with a worst-case upper bound of  $O(n^{10})$ . While this bound reflects adversarial symmetry cases, empirical behavior is substantially more favorable.

Across a diverse collection of graph families, including random graphs, highly regular constructions, and standard benchmark instances, the algorithm resolved all tested cases within prescribed refinement limits. These experiments suggest that multi-scale diffusion geometry captures structural distinctions that are often inaccessible to raw eigenvalues or purely combinatorial refinement methods.

Beyond graph isomorphism, this work establishes a concrete algorithmic role for discrete spectral geometry. Curvature, interpreted as a vector-valued multi-scale diffusion signature rather than a single scalar invariant, functions as a systematic driver of symmetry breaking. Fractional spectral scaling further links discrimination power to intrinsic spectral dimension, providing a principled mechanism for adapting diffusion behavior across graph families. This geometric viewpoint complements classical combinatorial and group-theoretic techniques and may inform related tasks such as canonical labeling, network alignment, and structural comparison.

Several directions merit further investigation. From an algorithmic standpoint, optimizing spectral computation, exploring sparse or iterative eigensolvers, and studying scalability to substantially larger graphs are natural next steps. From a theoretical perspective, characterizing graph classes for which diffusion-based refinement alone suffices, sharpening worst-case bounds, and clarifying the interaction between spectral scaling and automorphism group structure remain open problems.

The present results demonstrate that multi-scale diffusion geometry provides a robust and expressive framework for symmetry resolution in graphs. Whether this framework can be further strengthened to yield sharper theoretical guarantees remains an open question, but its algorithmic effectiveness and conceptual coherence suggest a promising direction for continued study.

## References

- [1] Alfred V. Aho, John E. Hopcroft, and Jeffrey D. Ullman. *The Design and Analysis of Computer Algorithms*. Addison-Wesley, 1974.
- [2] S. Alexander and R. Orbach. Density of states on fractals: “fractons”. *Journal de Physique Lettres*, 43:L625–L631, 1982.
- [3] Noga Alon and Vitali D. Milman.  $\lambda_1$  isoperimetric inequalities for graphs, and superconcentrators. *Journal of Combinatorial Theory, Series B*, 38(1):73–88, 1985.
- [4] László Babai. On the complexity of canonical labeling of strongly regular graphs. *SIAM Journal on Computing*, 9(1):212–216, 1980.
- [5] László Babai. Graph isomorphism in quasipolynomial time. *Proceedings of the 48th Annual ACM Symposium on Theory of Computing*, pages 684–697, 2016.
- [6] Michele Benzi, Daniela Bertaccini, Federico Durastante, and Ilaria Simunec. Non-local network dynamics via fractional graph laplacians. *Journal of Complex Networks*, 8(3):cnaa017, 2020.
- [7] Ginestra Bianconi. The spectral dimension of simplicial complexes. *Physical Review E*, 2019. States  $\rho(\mu) \sim \mu^{ds/2-1}$  for small eigenvalues in terms of spectral dimension.
- [8] R. Burioni and D. Cassi. Universal properties of spectral dimension. *Physical Review Letters*, 76:1091–1093, 1996.
- [9] J. S. Caughman and J. J. P. Veerman. Kernels of directed graph laplacians. *Electronic Journal of Combinatorics*, 13(R39):1–13, 2006.
- [10] Isaac Chavel. *Eigenvalues in Riemannian geometry*, volume 115. Academic press, 1984.
- [11] Fan R. K. Chung. *Spectral Graph Theory*, volume 92 of *CBMS Regional Conference Series in Mathematics*. American Mathematical Society, Providence, RI, 1997.
- [12] Karamatou Yacoubou Djima and Ka Man Yim. Power spectrum signatures of graphs. *arXiv preprint*, page arXiv:2503.09660v1, 2025.
- [13] Sourav Dutta and Arnab Bhattacharya. RSVP: Beyond weisfeiler–lehman graph isomorphism test. *CoRR*, abs/2409.20157, 2024. <https://arxiv.org/abs/2409.20157>.
- [14] Miroslav Fiedler. Algebraic connectivity of graphs. *Czechoslovak Mathematical Journal*, 23(2):298–305, 1973.
- [15] Alexander Gamkrelidze, Günter Hotz, and Levan Varamashvili. New invariants for the graph isomorphism problem. *CoRR*, abs/1212.3055, 2018. <https://arxiv.org/abs/1212.3055>.
- [16] Martin Grohe. Graph isomorphism, logic, and polynomial time. *Bulletin of Symbolic Logic*, 21(1):1–45, 2015.

- [17] John E. Hopcroft and James K. Wong. A linear time algorithm for isomorphism of planar graphs. *Proceedings of the Sixth Annual ACM Symposium on Theory of Computing*, pages 172–184, 1974.
- [18] Sungchul Hwang, Chang-Keun Yun, Byungnam Kahng, and Doochul Kim. Spectral dimensions of hierarchical scale-free networks with shortcuts. *Physical Review E*, 82:056110, 2010. Gives spectral dimension results for hierarchical scale-free networks including  $(u, v)$ -flowers.
- [19] Eugene M. Luks. Isomorphism of graphs of bounded valence can be tested in polynomial time. *Journal of Computer and System Sciences*, 25(1):42–65, 1982.
- [20] Sohir Maskey, Raffaele Paolino, Aras Bacho, and Gitta Kutyniok. A fractional graph laplacian approach to oversmoothing. In *Proc. 37th Int. Conf. on Neural Information Processing Systems (NeurIPS)*, 2023.
- [21] Naoki Masuda, Mason A. Porter, and Renaud Lambiotte. Random walks and diffusion on networks. *Physics Reports*, 716–717:1–58, 2017. Review; summarizes  $d_s$  for  $(u, v)$ -flowers and connects  $d_s$  to Laplacian scaling.
- [22] Naoki Masuda, Mason A. Porter, and Renaud Lambiotte. Random walks and diffusion on networks. *arXiv preprint arXiv:1612.03281v3*, 2020. Survey; reports spectral dimension formulas including  $d_s = 2 \ln(u + v) / \ln(uv)$  for fractal  $(u, v)$ -flowers.
- [23] Russell Merris. Laplacian matrices of graphs: a survey. *Linear Algebra and its Applications*, 197–198:143–176, 1994.
- [24] Subbaramiah Minakshisundaram and Åke Pleijel. Some properties of the eigenfunctions of the laplace-operator on riemannian manifolds. *Canadian Journal of Mathematics*, 1(3):242–256, 1949.
- [25] Bojan Mohar. The laplacian spectrum of graphs. *Graph Theory, Combinatorics, and Applications*, 1992. Survey on Laplacian eigenvalues and their interpretations.
- [26] Sara Najem, Dima Mrad, and Mohammad Elsayed. Geometric features of higher-order networks via the spectral triplet. *arXiv preprint arXiv:2509.04311*, 2025.
- [27] Peter Petersen. *Riemannian Geometry*. Springer, 3rd edition, 2016.
- [28] Dan Raviv, Ron Kimmel, and Alfred M. Bruckstein. Graph isomorphisms and automorphisms via spectral signatures. *IEEE Transactions on Pattern Analysis and Machine Intelligence*, 35(8):1985–1993, 2013.
- [29] Martin Reuter, Franz-Erich Wolter, and Niklas Peinecke. Laplace–beltrami spectra as shape-dna of surfaces and solids. *Computer-Aided Design*, 38(4):342–366, 2006.
- [30] Hernán D. Rozenfeld, Reuven Cohen, Daniel ben Avraham, and Shlomo Havlin. Deterministic scale-free networks. *Journal of Physics A: Mathematical and Theoretical*, 43(42):425004, 2010.
- [31] Hernán D. Rozenfeld, Chaoming Song, and Hernán A. Makse. Small-world to fractal transition in complex networks: a renormalization group approach. *Physical Review Letters*, 98(12):128701, 2007.
- [32] Jian Sun, Maks Ovsjanikov, and Leonidas Guibas. A concise and provably informative multi-scale signature based on heat diffusion. *Computer Graphics Forum*, 28(5):1383–1392, 2009.

- [33] Joaquín J Torres and Ginestra Bianconi. Simplicial complexes: higher-order spectral dimension and dynamics. *Journal of Physics: Complexity*, 1(1):015002, 2020.
- [34] Ryuhei Uehara, Seinosuke Toda, and Akira Nagoya. Tractable and intractable instances of the graph isomorphism problem. *Theoretical Computer Science*, 349(2):243–256, 2005.
- [35] Adrien Weihs and Matthew Thorpe. Consistency of fractional graph-laplacian regularization in semi-supervised learning with finite labels. *SIAM Journal on Mathematical Analysis*, 56(4), 2024.
- [36] Boris Weisfeiler and Andrei Leman. Reduction of a graph to a canonical form and an algebra arising during this reduction. *Nauchno-Technicheskaya Informatsia*, 2:12–16, 1968.
- [37] Mengjie Zhang, Yong Lin, and Yunyan Yang. Fractional laplace operator and related schrödinger equations on locally finite graphs. *Calculus of Variations and Partial Differential Equations*, 64:227, 2025.
- [38] Mengjie Zhang, Yong Lin, and Yunyan Yang. Fractional laplace operator on finite graphs. *Revista Matemática Complutense*, 2025. Published online 11 Nov 2025.